



저작자표시-비영리-변경금지 2.0 대한민국

이용자는 아래의 조건을 따르는 경우에 한하여 자유롭게

- 이 저작물을 복제, 배포, 전송, 전시, 공연 및 방송할 수 있습니다.

다음과 같은 조건을 따라야 합니다:



저작자표시. 귀하는 원저작자를 표시하여야 합니다.



비영리. 귀하는 이 저작물을 영리 목적으로 이용할 수 없습니다.



변경금지. 귀하는 이 저작물을 개작, 변형 또는 가공할 수 없습니다.

- 귀하는, 이 저작물의 재이용이나 배포의 경우, 이 저작물에 적용된 이용허락조건을 명확하게 나타내어야 합니다.
- 저작권자로부터 별도의 허가를 받으면 이러한 조건들은 적용되지 않습니다.

저작권법에 따른 이용자의 권리는 위의 내용에 의하여 영향을 받지 않습니다.

이것은 [이용허락규약\(Legal Code\)](#)을 이해하기 쉽게 요약한 것입니다.

[Disclaimer](#)

이학석사 학위논문

Lattice preferred orientation of
talc and implications for seismic
anisotropy in subduction zones

활석의 격자선호방향과 이것이
섭입대의 지진파 비등방성에 미치는 영향

2016 년 8 월

서울대학교 대학원

지구환경과학부

이 정 진

Abstract

Lattice preferred orientation of talc and implications for seismic anisotropy in subduction zones

Jungjin Lee

School of Earth and Environmental Sciences

The Graduate School

Seoul National University

Talc is one of the important hydrous phyllosilicates formed in the mantle wedge and deep oceanic slab in subduction zones. Hydrous minerals have been suggested as a representative factor for high seismic anisotropy and large delay time observed in some subduction zones. Even though a strong lattice preferred orientation (LPO) of the hydrous minerals has been known to increase seismic anisotropy in the upper mantle and subducting slab, the LPO of naturally deformed talc has not been reported. In this study, LPO of talc in high/ultrahigh pressure metamorphic schist samples was measured and the resultant seismic anisotropy of polycrystalline talc was calculated using the pressure-dependent elastic constants of single-crystal talc. The LPO results showed that talc had strong alignment of [001] axes subnormal to the foliation and weak girdle

of [100] and [010] axes subparallel to the foliation with a weak concentration. The calculated seismic anisotropy of talc was high (68–69 % for P–wave and 21–23 % for S–wave) and it was decreased with increasing pressure. The polarization direction of vertically penetrating fast S–wave of talc was trench–parallel with the dipping angle of slab over 30 degrees. The V_{s1} polarization direction of talc also varied with the LPO of talc [100] axes and [010] axes.

Our results reveals that the presence of a strong LPO of talc in subduction zone would account for the observation of large delay time (1–2 sec) which is difficult to be explained by only the dominant mantle phase olivine. On the other hand, the LPO of talc could be an important factor to trench–parallel seismic anisotropy of fast S–wave observed in many subduction zones.

Keywords : talc, lattice preferred orientation, seismic anisotropy, subduction zone

Student Number : 2014–20324

Contents

Abstract	i
Contents	iii
List of tables	v
List of figures	vi
Chapter 1. Introduction.....	1
Chapter 2. Previous studies.....	4
Chapter 3. Geological setting.....	6
3.1. Locality and previous field study	6
3.2. Previous kinematic analysis about subduction– exhumation mechanism	8
Chapter 4. Sample description.....	11
Chapter 5. Methods.....	18
5.1. LPO measurement.....	18
5.2. Calculation of elastic constant of talc and bulk rock seismic anisotropy	19
Chapter 6. Results	23
6.1. LPO measurements	23
6.2. Seismic properties of talc and other composite minerals	28
6.3. Seismic anisotropy of talc at high pressures.....	36

Chapter 7. Discussion.....	41
7.1. LPO of talc in subduction zone.....	41
7.2. Seismic anisotropy of polycrystalline talc	42
7.2.1. Effect of LPO of talc on seismic anisotropy	42
7.2.2. Effect of pressure on seismic anisotropy of talc.....	
.....	48
7.2.3. Effect of subducting angle on seismic anisotropy of	
talc	54
Chapter 8. Conclusion.....	61
References.....	62
국문 초록	79

List of tables

Table 1. Modal composition of major composite minerals in Grt–Cld–Tlc schist samples and average grain size of talc and chloritoid.	15
Table 2. Seismic anisotropy result for each composite mineral and whole rock composition of the three Grt–Cld–Tlc schist samples.	44
Table 3. Calculated seismic anisotropy of talc using the pressure–dependent elastic constant and the LPO of talc measured in each Grt–Cld–Tlc sample.	46

List of figures

Figure 1. (a) Location of Tianshan and generalized tectonic division of the western Tianshan. (b) Geologic map of the Makbal UHP metamorphic complex. (c) The cross section along line A–A' within the (U)HP Makbal formation.	7
Figure 2. (a) Photographs of some strongly deformed garnet–chloritoid–talc schist samples investigated in this study.	12
Figure 2. (b–d) Thin sections show the matrix minerals of the three schists. (b) 15R, (c) 10–16, and (d) 12–52.	13
Figure 2. (e–f) (e) Possible quartz pseudomorph after coesite in the garnet (10–16), showing radiating cracks. (f) Extinction of talc grains in sample 12–52 (XPL).	14
Figure 3. Contoured pole figures show LPO patterns of talc in the three Grt–Cld–Tlc schist samples.	24
Figure 4 (a) LPO patterns of phengite and chlorite in the sample 15R and 10–16.	25
Figure 4 (b) Contoured pole figures show LPO patterns of chloritoid in the three Grt–Cld–Tlc schist samples.	27

Figure 4 (c). LPO patterns of garnet porphyroblasts and weak LPO pattern of quartz in the three samples.	29
Figure 5. P–wave velocity, S–wave anisotropy, and the polarization directions of the fast S–wave for talc at zero pressure.	30
Figure 6 (a) P–wave velocity, S–wave anisotropy, and the polarization directions of the fast S–wave of phengite and chlorite in the two samples 15R and 10–16 at ambient pressure.	31
Figure 6 (b) P–wave velocity, S–wave anisotropy, and the polarization directions of the fast S–wave of garnet and quartz in the three samples at ambient pressure.	32
Figure 7. Seismic velocities and anisotropy from the mixture of composite minerals (talc, phengite, chlorite, garnet and quartz) in the three Grt–Cld–Tlc schist samples.	34
Figure 8. Relationship of hydrous mineral content and seismic anisotropy of the Grt–Cld–Tlc schist.	35
Figure 9. (a–c) P–wave velocity, S–wave anisotropy, and the polarization directions of the fast S–wave of talc with the elastic constants for the pressure (a) 0.9 GPa, (b) 2.9 GPa, (c) 5.0 GPa.	38

Figure 10. Single crystal P–wave velocity, S–wave maximum anisotropy, and the polarization directions of the fast S–wave of monoclinic talc.	43
Figure 11. Plot of seismic anisotropy of polycrystalline talc in the Grt–Cld–Tlc schists and single–crystal talc as a function of pressure.	49
Figure 12. Variation on the polarization directions of fast S–wave as a function of the given pressures.	52
Figure 13. Anisotropic thickness of talc and olivine as a function of delay time.	55
Figure 14. Seismic anisotropy of talc (sample 10–16) in response to the change of subduction dipping angle at the pressure of 2.9 GPa.	57
Figure 15. Delay time/thickness of anisotropic layer for the case of 100 % talc.	59

Chapter 1. Introduction

Seismic anisotropy has been observed in many subduction zones and can be largely affected by the elasticity and the lattice preferred orientation (LPO) of each composite mineral (Long and Silver, 2008; Long and van der Hilst, 2006; Park and Levin, 2002; Russo and Silver, 1994). The anisotropy of shear waves can be induced by the preferential alignment of the rock's composite minerals in the Earth's interior (Karato et al., 2008; Mainprice et al., 2000). Anisotropic field in subduction zones would vary throughout the four-layered structure of subduction zones: the sub-slab mantle, the slab, the mantle wedge, and the overlying plate. Since olivine is the primary mineral in the mantle, the LPO of olivine has been considered as an important factor which control the trench-parallel seismic anisotropy in subduction zones (Jung and Karato, 2001; Jung et al., 2006; Jung et al., 2014; Karato et al., 2008; Long and Silver, 2008; Zhang and Karato, 1995). On the other hand, hydrous minerals such as talc, serpentine, and mica are also present in the mantle wedge and oceanic slab. Those minerals have been known as elastically very anisotropic materials, so the LPO of those minerals has been suggested to cause high seismic anisotropy in subduction zones (Bezacier et al., 2010; Chheda et al., 2014; Jung, 2011; Mainprice and Ildefonse, 2009; Nishizawa and Yoshino, 2001).

Talc is a common hydrous magnesium silicate in the olivine-

rich mantle together with serpentine, and it has been suggested as an exceptionally anisotropic material in subduction zones (Mainprice et al., 2008). Representative mechanisms of talc formation at the mantle have been reported as silica–metasomatism of serpentine at the base of the hydrated mantle wedge (Bach et al., 2004; Bailey and Holloway, 2000; Mainprice and Ildefonse, 2009; Peacock and Hyndman, 1999). The breakdown of antigorite in the serpentinized mantle wedge also gives the assemblage of olivine + talc + water and in this case talc can represent up to 41 % by volume of the rock under the pressures <1.5 GPa and temperatures 500–650 °C (Hacker et al., 2003; Ulmer and Trommsdorff, 1995). In the ultramafic oceanic slab metamorphosed at ultra–high pressure conditions (eclogites–facies), talc still be present even at water under–saturated conditions (Pawley and Wood, 1995; Poli and Schmidt, 1997). There are some talc–bearing high–ultrahigh pressure (UHP) Complex, e.g. the Bixiling mafic–ultramafic complex in the Dabie UHP metamorphic terrane (Liou and Zhang, 1995), Pinchi Lake area in the British Columbia (Ghent et al., 2009), accompanying other eclogite–facies phases such as glaucophane, lawsonite, paragonite, phengite, and chloritoid. The amount of talc inherited from hydrothermal alteration of the mafic oceanic crust can be more than 10% along the slab (Boschi et al., 2006; Escartín et al., 2003). Several experimental studies have also suggested a wide P–T range of stability of talc extending up to eclogite–facies, temperature of 700–800 °C at the pressure of 5 GPa (Moore and Lockner, 2011; Pawley and Wood, 1995). Therefore, talc is one of

the last forming phyllosilicates during prograde metamorphism at subduction zones and it makes talc of potential significance at a wide range of seismogenic depths.

However, no quantitative measurements of the LPO of talc has been reported although that of anisotropic serpentine has been studied well (Bezacier et al., 2010; Jung, 2011; Katayama et al., 2009). In this study, the LPO of talc in the garnet–chloritoid–talc schist from the Makbal UHP Complex was measured and the seismic properties of talc at high–ultrahigh pressures were calculated using the elastic constants of single–crystal talc. The LPO of talc would be relatively simple to understand with the alignment of their basal planes due to its platy habit. Given its high anisotropy, it would have an important role on the seismic anisotropy of oceanic slab as well as that of the overlying mantle wedge. The LPO of talc and the pressure–induced variations in the elastic properties of talc could help to understand the observation of seismic anisotropy and polarization direction of fast shear wave at supra–subduction zones at elevated pressures.

Chapter 2. Previous studies

Many previous studies have focused on the role of talc as frictionally weak material of stable–sliding behavior at the mantle wedge and upper slab (Escartin et al., 2008; Hirauchi et al., 2012; Misra et al., 2014; Moore and Lockner, 2008; Moore and Rymer, 2007; Peacock and Hyndman, 1999), or as a low–velocity mineral at the upper slab interface (Bailey and Holloway, 2000; Connolly and Kerrick, 2002; Kim et al., 2013). Metasomatic growth of talc–rich layer at the bottom of the serpentized mantle wedge has been proposed as fault–zone weakening process in some subduction fault–zones. Therefore, several previously reported works have focused on the microstructural evolution of talc and basal glide of talc occurring at various tectonic settings. The frictional rupture experiments on talc found that the weakening effect of talc was stronger than serpentine, and that the degree of weakening is increased with increasing temperature and increasing amount of talc (Hirauchi et al., 2012; Moore and Lockner, 2008). One torsion experiment conducted on synthetic talc showed strain–rate hardening followed by brief weakening events, and friction evolution of talc which was interpreted as brittle–ductile transition (Misra et al., 2014). A depth condition of brittle–ductile transition of talc was previously determined as temperature of 400–600 °C and confining pressure of 300 MPa by a triaxial compression experiment (Escartin et al., 2008). The low frictional coefficient of talc found

by those experimental studies can be related to slow-slip events (SSE) and aseismic slip observed at some subduction zones (Song and Kim, 2012; Wang et al., 2009). Particularly, talc has been regarded as an important mineral phase for aseismic slip in shallow (< 60 km) crustal fault within subduction zones such as Izu-Bonin-Mariana (Wang et al., 2009) and Mexican subduction zone (Kim et al., 2013).

There are some petro-structural studies about the global metapelitic schist worldwide and they have measured preferred orientation of phyllosilicates such as muscovite, biotite, illite, chlorite, and kaolinite (Haerinck et al., 2015; Kim and Jung, 2015; Wenk et al., 2010). Those crystallographic preferred orientation (CPO) of hydrous clay minerals in crustal schist has been regarded to cause seismic anisotropy in various tectonic shear zones (Godfrey et al., 2000). However, the CPO (or LPO) of talc evolved in a deformed shear zone has not been measured yet, although some deformation experiments reported high strain crystal textures of talc. For talc, the CPO has been thought to cause seismic anisotropy associated with SSE beneath the mantle wedge (Song and Kim, 2012). In this proposal, in order to establish the effect of talc LPO on seismic anisotropy in subduction zones, the ultra-high pressure (UHP) talc-bearing schist was analyzed and it could also provide seismic implication about the talc layer formed at UHP subducted oceanic slab as well as at the mantle wedge of the lower pressure.

Chapter 3. Geological setting

3.1. Locality and previous field study

The investigated rock samples were Garnet–Chloritoid–Talc schist (in the following termed Grt–Cld–Tlc schists) which was collected from the UHP Makbal Complex, northern Tianshan of Kazakhstan and Kyrgyzstan (Fig. 1). The Tianshan orogen is a part of the Alpine–Himalaya collision belt as well as of the Central Asian Orogenic Belt (CAOB) (Allen et al., 1993; Klemd et al., 2015; Windley et al., 1990). This orogenic belt was formed by lateral accretion of magmatic arcs and microcontinents, as well as vertical accretion of mantle–derived material to the crust (Kröner et al., 2007; Long et al., 2011; Xiao and Santosh, 2014; Zhou and Wilde, 2013). Enclosed within the Tianshan orogen are a number of (ultra)high pressure metamorphic complexes. The Makbal UHP Complex among them is located in the Northwestern Tianshan and comprises areas on both sides of the Kazakh–Kyrgyz border (Fig. 1). The Makbal Complex is the tectonic mélangé related to convergence and subduction of the Kyrgyz–Terskey ocean (between the Middle Tianshan and the Northern Tianshan) under the southwestern margin of the Northern Tianshan during the Early Ordovician and closing of the ocean during the Late Ordovician (Alexeiev et al., 2011; Klemd et al., 2015; Kröner et al., 2013; Meyer et al., 2014). The central Makbal Complex was interpreted

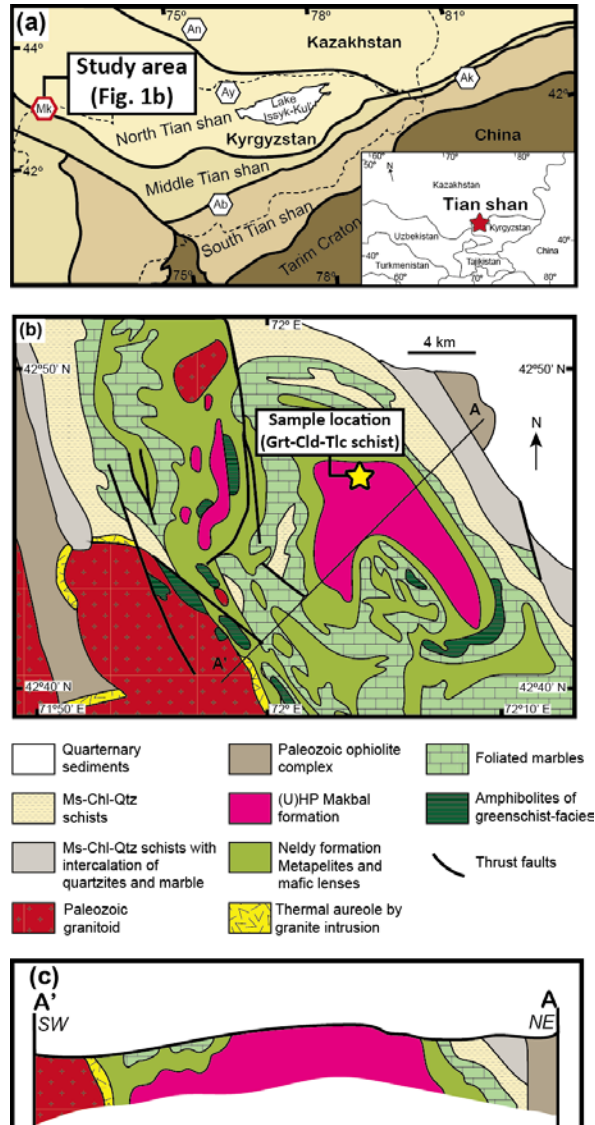


Figure 1. Location of Tianshan labelled as red star and generalized tectonic division of the western Tianshan. Labeled hexagons are UHP complexes in the local area and the location of the study area (MK: Makbal complex) is labelled as red hexagon. Modified after Orozbaev et al. (2015). (b) Geologic map of the Makbal UHP metamorphic complex modified after Orozbaev et al. (2015). (c) The cross section along line A–A’ within the (U)HP Makbal formation. The ‘dome–like structure of exhumation was suggested by previous studies (Tagiri et al., 2010).

to represent a tectonic mélangé of quartzites, metapelites, and UHP Grt–Cld–Tlc schists that incorporated exotic blueschist–eclogite blocks (Konopelko et al., 2012; Meyer et al., 2013; Orozbaev et al., 2015; Tagiri et al., 2010; Togonbaeva et al., 2009). Recent studies on the Makbal complex in the Northern Tianshan suggested that the mafic blocks are dismembered fragments of the oceanic slab which were captured in different depths in the subduction zone and that the depth from which those blocks had been exhumed (70–85 km) are shallower than that from which the Grt–Cld–Tlc schist (\approx 95 km) (Meyer et al., 2014; Meyer et al., 2013; Orozbaev et al., 2015).

3.2. Previous kinematic analysis about subduction-exhumation mechanism

There are some previous petrological researches about the Grt–Cld–Tlc schist in the Makbal complex and they focused on the subduction–exhumation history of the Grt–Cld–Tlc schist associated with the adjacent blueschist–eclogite rocks. A recent study interpreted the protolith of the Grt–Cld–Tlc schist in the Makbal complex as intensely metasomatized mafic igneous rock at oceanic basin by high–temperature seafloor alteration, based on geochemical analysis reporting significantly lower contents of alkali elements and CaO and higher mafic components (MgO and Fe₂O₃) comparing to the geochemistry of MORB and OIB, as well as the

strong variation of SiO_2 (Meyer et al., 2014). Peak metamorphic conditions of the Grt–Tlc–Cld schist from the Makbal Complex therefore were determined as the ultra–high pressure and low temperature; $P = 2.7\text{--}3.2$ GPa in a range of $T = 530\text{--}580$ °C (Orozbaev et al., 2015), $P \approx 2.85$ GPa and $T \approx 580$ °C by using a detailed pseudosection analysis with several mineral isopleths; Si–isopleth of phengite, X_{Mg} of talc, and $X_{\text{Fe}^{2+}}$ of chloritoid (Meyer et al., 2014). Those studies also found the mineral assemblage of the peak metamorphism as coesite + garnet + chloritoid + talc + phengitic mica + rutile. The garnet + chloritoid + talc assemblage is constrained by the expense of chlorite, lawsonite, and quartz around $P = 2.0\text{--}2.5$ GPa and $T = 500\text{--}560$ °C, indicated by the petrogenetic grid for the NCKFMASH system (Wei and Powell, 2006).

Chen et al. (2013) reported that the high amount of low–density HP–UHP hydrous minerals such as phengite and talc in low– T eclogites can facilitate the exhumation of deeply subducted crust with MORB composition under the condition of eclogite–facies up to depths of ≈ 110 km along a cold subduction path with a geotherm of 6 °C/km. In the same study, talc was investigated to be preserved at the pressure of up to 3.6 GPa along the cold geotherm. On the other hand, the previous researches about the occurrence of coesite relict in the garnet rim of the Grt–Cld–Tlc schists (Konopelko et al., 2012; Meyer et al., 2014; Orozbaev et al., 2015; Tagiri et al., 2010; Togonbaeva et al., 2009) have indicated

continental-type UHP subduction of the central Makbal Complex. Because UHP minerals are rarely preserved after exhumed from the depth of 100–200 km, the coesite relict in the garnet rim can be explicable through rapid exhumation, rapid cooling during decompression before thermal relaxation could heat the cold subducted material enough to induce melting (Winter, 2010). Little deformation and fluid-absent condition may be also required for the preservation of the UHP mineral (Guillot et al., 2009).

For the Makbal UHP Complex (Fig. 1), the structural antiform or ‘dome’ formation of exhumation (Tagiri et al., 2010) and such UHP dome has been thought to be exhumed rapidly in a buoyant channel flow from the depth of > 100 km subduction channel (Beaumont et al., 2009). Indeed, numerical and analog experiments show the efficacy of buoyancy as an exhumation mechanism (Beaumont et al., 2009; Gerya et al., 2002). Such an exhumation mechanism about channel flow is similar to the serpentinite-type subduction channels, however the occurrence of serpentinite in the Makbal complex has not been reported. Now, seismic tomography models have suggested only thick crust beneath the Tianshan as a result of underthrusting of the Tarim Basin beneath the Tianshan crust, and it refers to the end of exhumation under the Northern Tianshan (Gilligan et al., 2014; Vinnik et al., 2006; Wolfe and Vernon, 1998).

Chapter 4. Sample description

Three Grt–Cld–Tlc schist samples (15R, 10–16, 12–52) from the Makbal Complex were chosen to study. Porphyroblastic garnet grains have large average diameter of about 1.2 cm (Fig. 2a). They contain various kinds of solid inclusions of quartz, chloritoid, talc, rutile, and apatite. The garnet porphyroblasts are embedded in a matrix of talc, chloritoid, chlorite, phengitic mica, quartz, minor rutile, and accessory apatite and glauconite. There was no lawsonite, glaucophane, or omphacite which are also blueschist–eclogite facies minerals but contain calcium element. Mineral volume fractions and average grain sizes for each mineral were determined by modal abundance in thin section (Table 1). Even though the mineral modal proportions of three samples are different from each other, they have almost same composite mineral assemblages which represent the peak metamorphic minerals of the Grt–Cld–Tlc schist (e.g. talc, phengite, chloritoid, garnet, rutile, etc.; Meyer et al., 2014). The foliation of the schist is well–defined by talc flakes, one of the abundant matrix minerals. Elongated chloritoid, rutile, and some platy mineral grains commonly indicated the lineation of each schist sample. Other matrix phyllosilicate grains such as talc, phengite, and chlorite were almost oriented subparallel to the determined lineation, might because of the slight rotation effect of pressure shadow of large porphyroblastic garnet.



Figure 2. (a) Photographs of some strongly deformed garnet–chloritoid–talc schist samples investigated in this study (upper: 10–16, lower: 12–52). Elongated green–grey chloritoid and opaque white talc define the foliation of the rock. The coin scale represents 2.2 cm. Red arrows indicate the garnet porphyroblasts (maximum $d = 1.7$ cm).

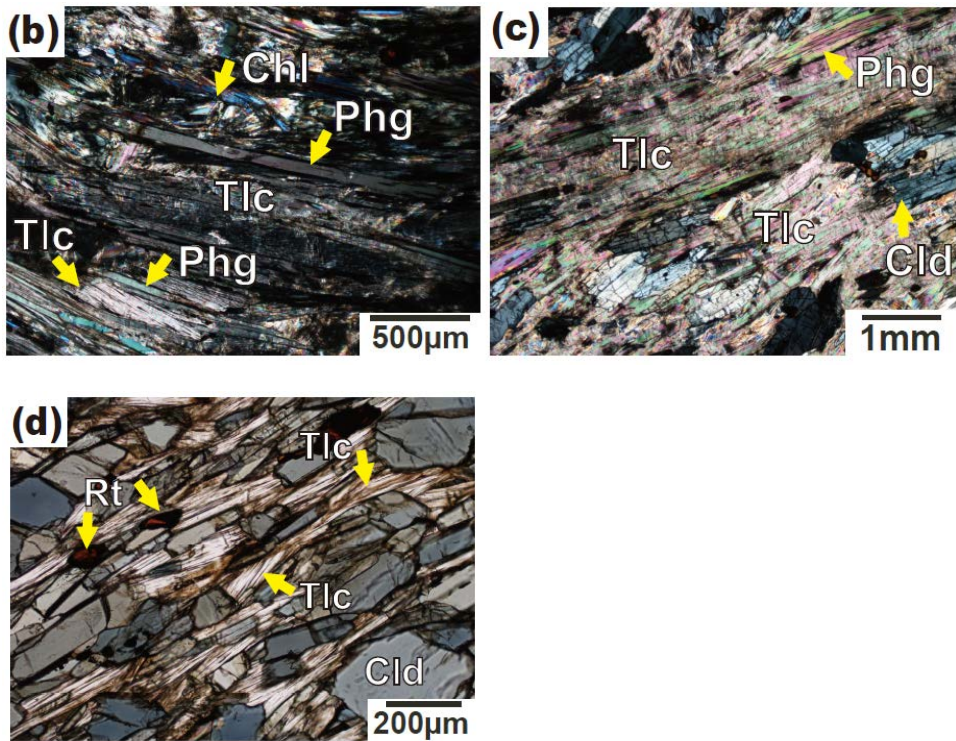


Figure 2. (b–d) Thin sections show the matrix minerals of the three schists. (b) 15R, (c) 10–16, and (d) 12–52. (b) Elongated talc showing pearly luster and phengitic mica laths (XPL). In the chlorite–rich sample, chlorite showing pleochroism of brownish green seems to replace chloritoid. (c) Well–elongated talc grains and aggregation of chloritoid (XPL). Some chloritoid grains show twinning and cleavages. (d) Relatively short flakes of talc and regular rounded shape of chloritoid (PPL). In addition, the average grain size of the sample 12–52 is smaller than that of other two samples. Tlc: talc, Phg: phengite, Chl: chlorite, Cld: chloritoid, Rt: rutile.

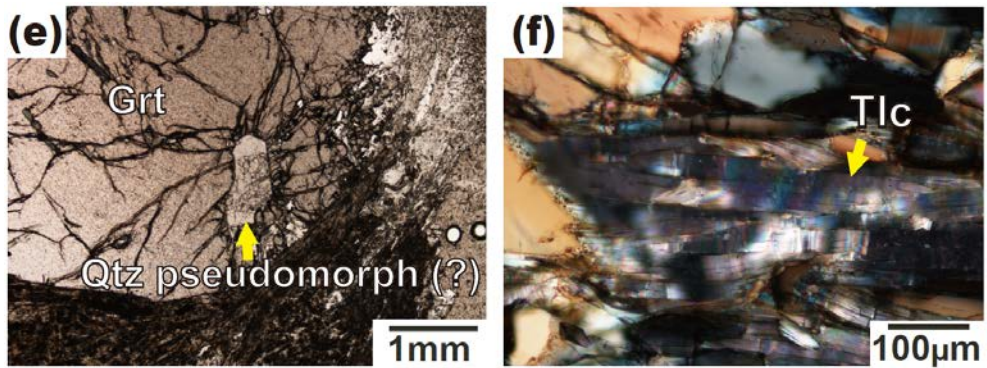


Figure 2. (e–f) (e) Possible quartz pseudomorph after coesite in the garnet (sample 10–16), showing radiating cracks. (f) Extinction of talc grains in sample 12–52 (XPL). This plastic deformation feature of talc is observed in the three schist samples.

Table 1. Modal composition of major composite minerals in Grt–Cld–Tlc schist samples and average grain size of talc and chloritoid.

Sample	Modal composition (vol. %)						Avg. grain size of talc (mm) ^a	Avg. grain size of chloritoid (mm) ^b
	Talc	Chloritoid	Chlorite	Phengite	Quartz	Garnet		
15R	25	10	30	10	15	10	1.8	0.34
10-16	40	20	5	7	3	25	1.6	0.41
12-52	20	25	2	1	17	35	0.45	0.10

^a Average grain size was determined by measuring the length of major axes of over 100 talc grains and arithmetically averaging them.

^b Average grain size was determined by measuring the area of over 100 chloritoid grains and calculating the diameter of the arithmetically averaged grain area. The method that measure the area rather than the length of each grain is because of their irregular grain shape.

Talc (21–39 vol. %) is anhedral and highly foliated with flake-like shape (Figs. 2b–2d). Acicular and fibrous grains of phengite (<1–7 vol. %) are associated with talc in the matrix and more euhedral than talc. Chlorite (2–30 vol. %) shows greenish color in PPL and is ellipsoidal or ‘mushy’ in shape rather than its common bladed grain shape (Fig. 2b). This feature occurs as a secondary phase which could be retrograded from garnet rim and chloritoid, and is especially abundant in the sample 15R (\approx 30 vol. %). Matrix platy chloritoid (10–26 vol. %) grains are subhedral and occur in bimodal grain sizes among the three schist samples. In two samples (15R and 10–16), chloritoid shows larger grain sizes forming irregular and massive aggregates. In the other small grain-sized sample (12–52), on the other hand, matrix chloritoid occurs as circular, pebble-like shape regularly (Fig. 2d). Granular quartz (3–18 vol. %) is anhedral and fills up the interspace between narrow and bladed phyllosilicate grains. Minor rutile grains are scattered as tiny ellipsoids in the matrix and as inclusions in garnet. Apatite has clear polygonal shape and is very rarely observed in the matrix and the garnet porphyroblasts as accessory Ca-bearing mineral.

The retrograde evolution of the samples is difficult to constrain, because it is like the only mineral grown during retrograde exhumation is chlorite replacing garnet and chloritoid. Another possible preserved evidence for retrogression is quartz pseudomorph after coesite, however it was not confirmed in this

study. The existence of UHP minerals (coesite relicts) in the garnet from the Grt–Cld–Tlc schist in the Makbal Complex has been observed as mentioned above, which indicates the maximum depth of subduction over 90–95km (Kotková et al., 2011; Wilke et al., 2015). In this study so far, a few of quartz grains with radiating crack textures were just observed in the garnet rim, which probably infer retrograded pseudomorphs after coesite (Fig. 2e). Talc, chloritoid and quartz show a distinct extinction (the feature of talc is in Figure 2f) and chessboard subgrain boundaries in quartz are also observed as strong deformation features.

Chapter 5. Methods

5.1. LPO measurement

The LPOs of talc and other major composite minerals (garnet, chlorite, phengitic mica, chloritoid and quartz) were determined by using electron backscattered diffraction (EBSD) in scanning electron microscope (SEM). JEOL JSM-6380 SEM housed at the School of Earth and Environmental Sciences (SEES) at Seoul National University (SNU) was used. To have the surface of talc grains smooth enough to be detected by electron beam, each thin section of the rock samples was polished carefully using syton colloidal silica for over 7 hours. The JEOL JSM-6380 SEM was operated at 20 kV accelerating voltage and 15mm working distance. Indexing EBSD patterns was done using HKL Channel 5 software. This software needs some input data including the crystal structure of analyzed mineral, and this crystallographic data of talc was taken from the work of (Mainprice et al., 2008). The area of LPO analysis was the matrix rather than the area closely adjacent to the large garnet grains, in order to ignore the distorted grains most of which belong to pressure shadow accompanying the garnet porphyroblasts in the Grt-Cld-Tlc schist.

5.2. Calculation of elastic constant of talc and bulk rock seismic anisotropy

Seismic properties of constituent minerals can be calculated by their intrinsic elastic properties. The essential elastic parameters include single-crystal elastic tensors (C_{ij}), mineral density, orientations of individual grains (available from SEM/EBSD analysis), and mineral modal abundances. To calculate penetrating acoustic velocities (V_p , faster V_{s1} , and slower V_{s2}) and their anisotropy for each polycrystalline mineral, the practical petro-physical software developed by Mainprice (1990) was used. It enables to evaluate the macroscopic elastic tensor and the densities using the individual LPO patterns and modal volume fraction by averaging the elastic constants over all the crystalline structures within the polycrystalline aggregate. P-wave anisotropy (AV_p) was calculated as $AV_p (\%) = 100 \times [(V_{p_{max}} - V_{p_{min}})/V_{p_{mean}}]$, and S-wave anisotropy (AV_s) was also calculated as $AV_s (\%) = 100 \times [(V_{s1} - V_{s2})/V_{s_{mean}}]$. The elastic tensors of talc (Mainprice et al., 2008), white mica (Vaughan and Guggenheim, 1986), chlorite (Mookherjee and Mainprice, 2014), garnet (Jiang, 2004), and quartz (McSkimin et al., 1965) were used for the calculation of elastic anisotropy at ambient pressure.

The pressure-dependent elastic tensors of talc single crystal were previously estimated by performing ab-initio simulation

(Mainprice et al., 2008). To compute the elastic constant tensor by ab-initio method, the bulk compression behavior of talc crystal should be analyzed using the third-order Birch Murnaghan equation-of-state (Birch, 1978). There are some similar studies using the ab-initio method in order to investigate the elastic properties of hydrous sheet silicates such as antigorite (Mookherjee and Capitani, 2011), chlorite (Mookherjee and Mainprice, 2014), and also phlogopite mica (Chheda et al., 2014) and their seismic implications. Those previous studies have calculated seismic anisotropy by “first principle simulation” which analyzes compression behavior of hydrous mineral crystal (crystal structure parameters as a function of unit-cell volume). As a result, full elastic constant tensor is obtained by computational process which strains the crystal lattice positively/negatively and determines the variation in stress tensor in respect to the applied strain tensor. More details about the calculation of pressure- (or unit cell volume-) dependent elastic tensors using ab-initio method are described by some related studies (Mookherjee and Mainprice, 2014; Mookherjee and Stixrude, 2009).

To consider a wide pressure range of talc stability, four pressure conditions were once specified as 0 GPa (as a reference), 0.9 GPa, 2.9 GPa, and 5.0 GPa in this proposal and the seismic anisotropy of polycrystalline talc is calculated for each pressure. Elastic tensors were determined for the four given pressure in reference to a suite of previously estimated C_{ij} by Mainprice et al.

(2008). The choice of the pressures was based on previous experimental and theoretical studies about the stability of talc. At first, the pressure 0.9 GPa (40 km depth) was selected to be representative for talc stability field at the mantle wedge. And, the peak metamorphic pressure of 2.85 GPa (\approx 2.9 GPa) for the Grt–Cld–Tlc schist in the Makbal UHP Complex was analyzed by an earlier petrological research (Meyer et al., 2014). This value falls within the previously estimated peak pressure range of 2.8–3.3 GPa (Orozbaev et al., 2015) and the range of $P > 2.5$ GPa for the Grt–Cld–Tlc schists from the Makbal Complex (Tagiri et al., 2010). Lastly, 5 GPa (150 km depth) at 710 °C as the highest pressure condition where talc is stable and finally breaks down to the 10 Å phase was remarked through experimental studies (Pawley and Wood, 1995).

In order to compare the seismic anisotropic effect of talc in the Grt–Cld–Tlc schist to that of other composite layered silicates (phengite and chlorite), a varying trend of elastic anisotropy as a function of modal proportion of those three hydrous minerals was also calculated. For a simple calculation process, the zero pressure C_{ij} for all composite minerals in the Grt–Cld–Tlc schist were used. One sample (15R) was selected for this comparative analysis. The bulk rock mineralogy of the sample 15R was assumed to be composed of talc + phengite + chlorite + garnet + quartz (ignoring chloritoid, rutile, and apatite). Their modal fractions were recalculated for each interval of volume ratio, based on the original

modal fractions of the sample 15R.

Chapter 6. Results

6.1. LPO measurements

The LPO patterns of monoclinic talc were obtained and plotted in pole figures (Fig. 3). Three samples (15R, 10–16, 12–52) all had enough talc content to plot representative LPO pattern. Those samples showed [001] axes strongly aligned subnormal to the foliation and (110) poles distributed as a girdle subparallel to the foliation. The talc in our study showed two different LPO patterns of [100] axes and (010) poles. Two samples of 15R and 10–16 showed [100] axes aligned subparallel to the lineation with a weak girdle subparallel to the foliation, and (010) poles. On the other hand, sample 12–52 showed [100] axes strongly aligned at the center of pole figure and (010) poles aligned subparallel to the lineation with a weak girdle subparallel to the foliation.

The LPOs of phengite and chlorite are plotted in pole figures (Fig. 4a). The LPO measurements were conducted for one sample (15R) which had the largest amount of phengite and chlorite among the three samples. The phengite LPO of [001] axes are strongly aligned subnormal to the foliation and poles of (010) are aligned sub-parallel to the lineation. Poles of (110) are aligned as a weak girdle subparallel to the foliation with a concentration subnormal to the lineation, and [100] axes are concentrated subparallel to the

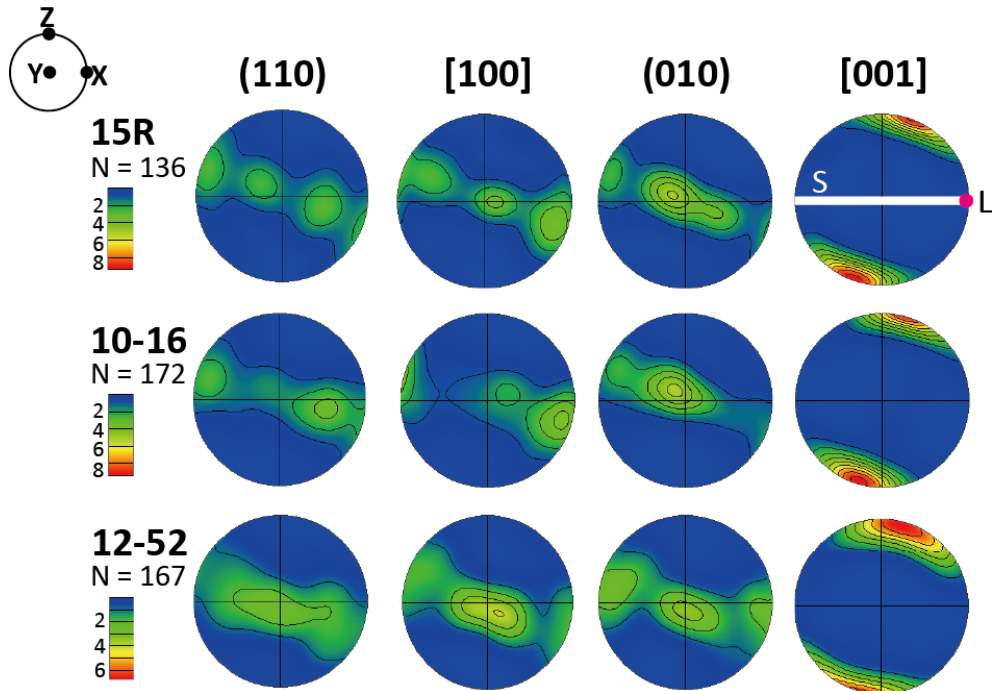


Figure 3. Contoured pole figures show LPO patterns of talc in the three Grt–Cld–Tlc schist samples, using an equal area, lower–hemisphere projection with 30° half width. Contours are multiples of uniform distribution (m.u.d.), a measure of LPO strength shown as colour bar. Each foliation (S) and lineation (L) is marked. The Z–direction is normal to the foliation and X–direction parallel to the lineation.

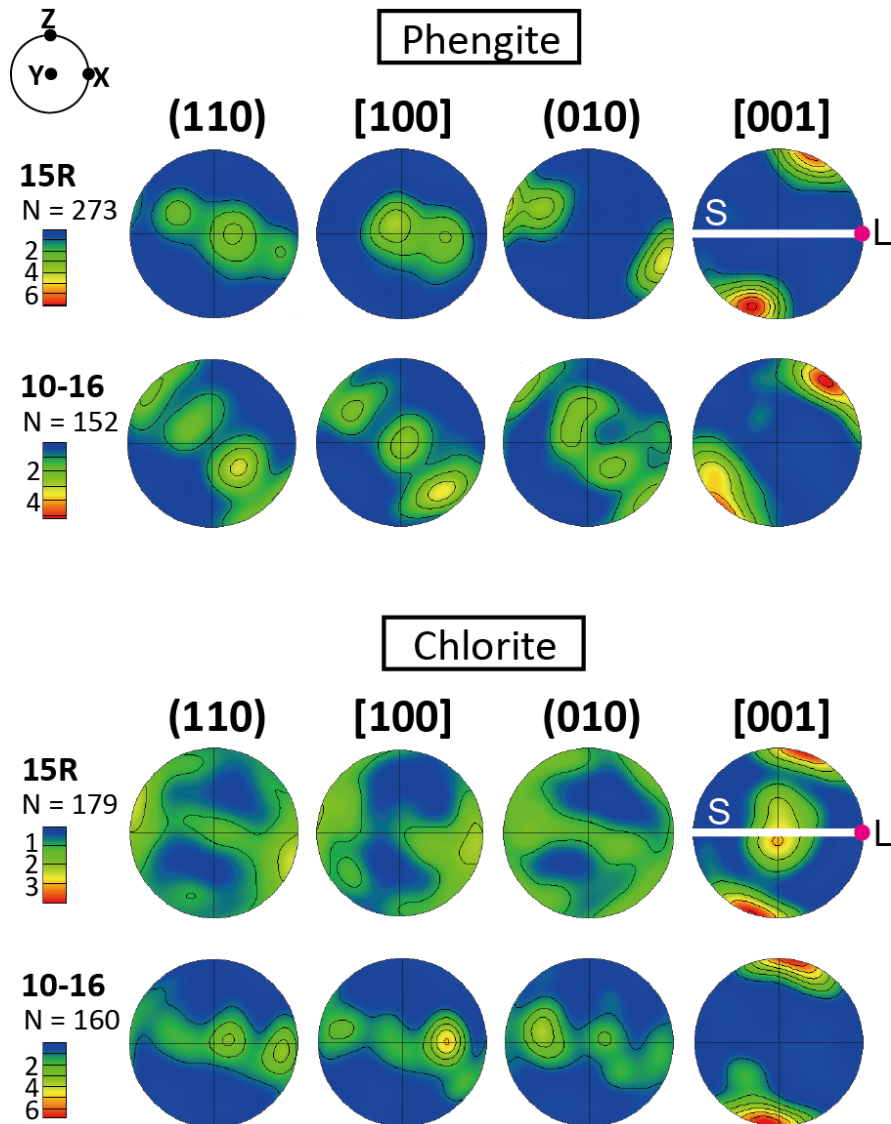


Figure 4 (a) LPO patterns of phengite and chlorite in the sample 15R. Pole figures using an equal area, lower-hemisphere projection with 30° half width. The Z-direction is normal to the foliation (S) and X-direction parallel to the lineation (L). LPO strength shown as colour bar is also marked. For both phengite and chlorite, pole figures of [001] have maximum concentration which is normal to the foliation.

foliation and subnormal to the lineation.

The chlorite LPO of [001] axes showed the maximum concentration subnormal to the foliation with a weaker concentration subnormal to the lineation, and both [100] axes and (110) poles are aligned subparallel to the lineation. The (010) poles showed a weak LPO with a girdle along the foliation. This pattern of chlorite LPO is similar to Kim and Jung (2015). The two hydrous phyllosilicates (phengite, chlorite) showed the common LPO concentration of the [001] axes normal or subnormal to the foliation (similar to talc LPO), which can be expected from their layered crystal structure. However, because chlorite is the secondary mineral of retrogression, the LPO of chlorite might be evolved later than that of talc or phengite.

The LPO of chloritoid (Fig. 4b) is similar to that of phengite and chlorite, with [001] axes oriented subnormal to the foliation. This feature was also reported previously (Haerinck et al., 2015). The other crystallographic axes showed different patterns respectively for each sample. In the sample 15R, (010) poles were aligned subparallel to the lineation, and (110) poles and [100] axes were weakly distributed subparallel to the lineation with a girdle along the foliation. In the sample 10–16, [100] axes were aligned subparallel to the lineation and poles of both (110) and (010) showed distribution normal to the lineation with a weak girdle along the foliation. In the sample 12–52, three crystallographic axes [110],

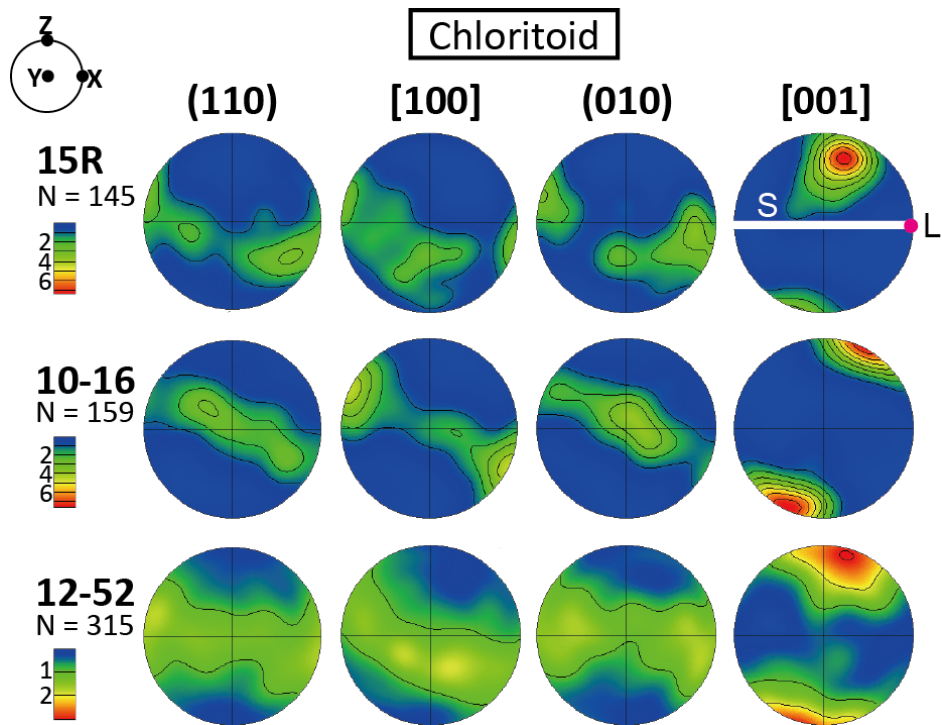


Figure 4 (b) Contoured pole figures show LPO patterns of chloritoid in the three Grt–Cld–Tlc schist samples, using an equal area, lower-hemisphere projection with 30° half width. LPO strength shown as colour bar is also marked. Each foliation and lineation is marked. Reference frame of pole figures is the same as in Fig. 4a.

[100], and [010] showed a girdle along the foliation without preferential concentration of the axes.

The LPOs of garnet porphyroblasts and quartz were examined and plotted in Figure 4c, which showed a distinctive pattern against the fabrics of talc, phengite and chlorite. Because garnet crystals are very large in size (7–17 mm), only a limited number of grains were analyzed in thin sections. The LPO patterns of garnet are nearly random, and that of quartz are much weaker relative to that of the layered silicates.

6.2. Seismic properties of talc and composite minerals

Seismic anisotropy of talc, phengite, chlorite, garnet, and quartz with LPO was calculated using the zero pressure elastic constants (Figs. 5, 6a, 6b). Note that the AVp of talc was significantly higher than that of both phengite and chlorite. For the case of talc, P-wave anisotropy (AVp) of talc was in the range of 68.1–69.1 % and the maximum shear wave anisotropy (AVs) in the range of 21.0–22.3 % (Fig. 5). For the other two composite phyllosilicates in the sample 15R, the AVp and maximum AVs were calculated as 36.1 % and 37.7 % for phengite, and 16.8 % and 23.9 % for chlorite, respectively (Fig. 6a). For the case of garnet and quartz, they showed very weak seismic anisotropy (Fig. 6b). The AVp was 0.8 % for garnet and 4.3 % for quartz, and the maximum AVs was

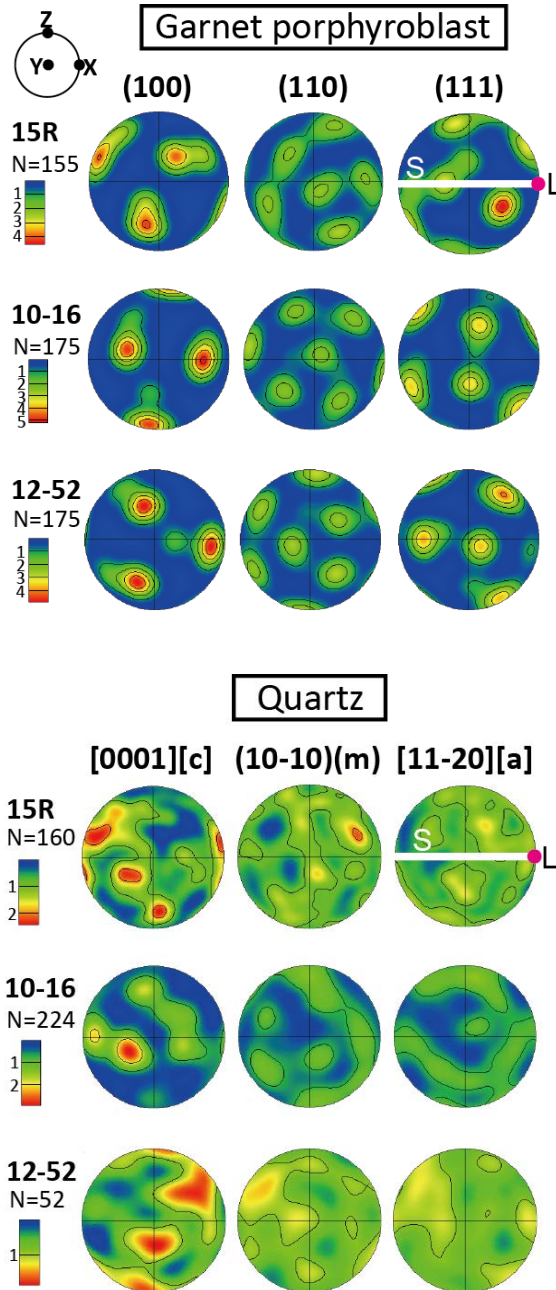


Figure 4 (c) LPO patterns of garnet porphyroblasts and weak LPO pattern of quartz in the three samples. Pole figures using an equal area, lower-hemisphere projection with 30° half width. LPO strength shown as colour bar is also marked. Reference frame of pole figures is the same as in Fig. 4a.

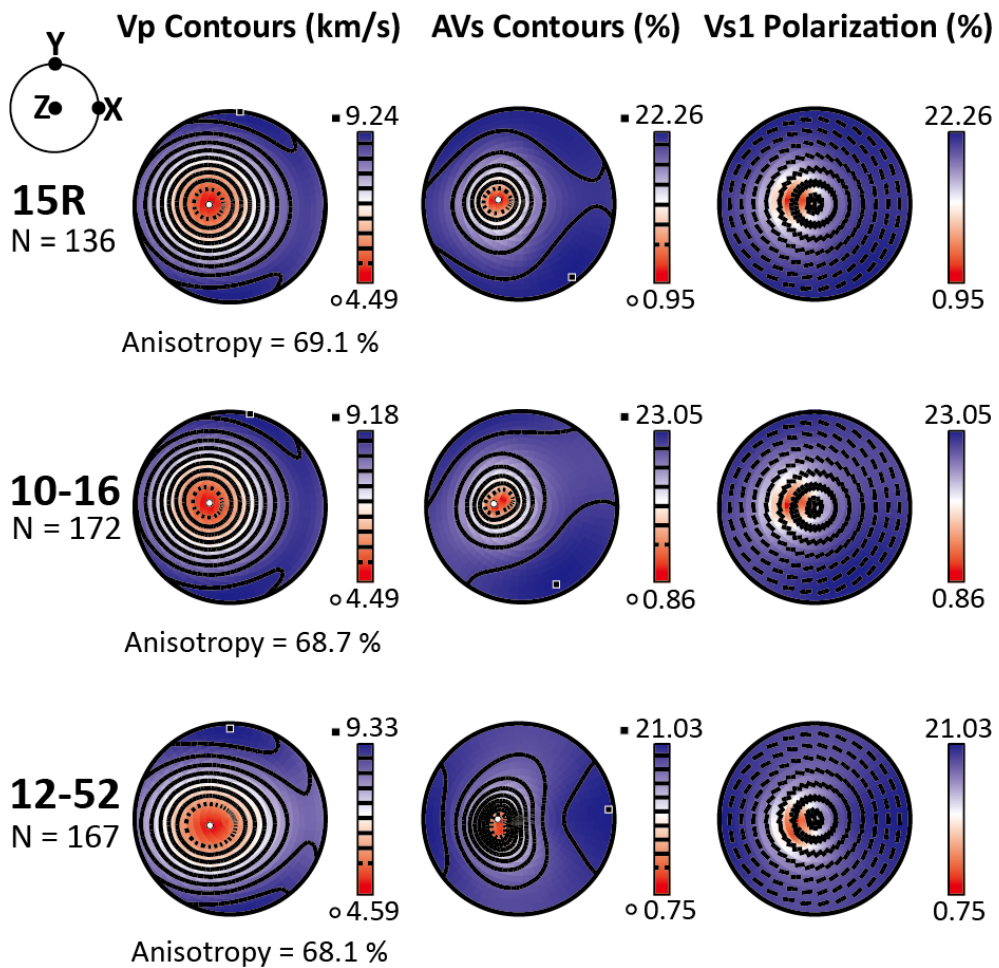


Figure 5. P-wave velocity, S-wave anisotropy, and the polarization directions (black lines) of the fast S-wave for talc at zero pressure. Reference frame is marked at top left. The X- and Z-directions represent lineation and the direction normal to the foliation, respectively.

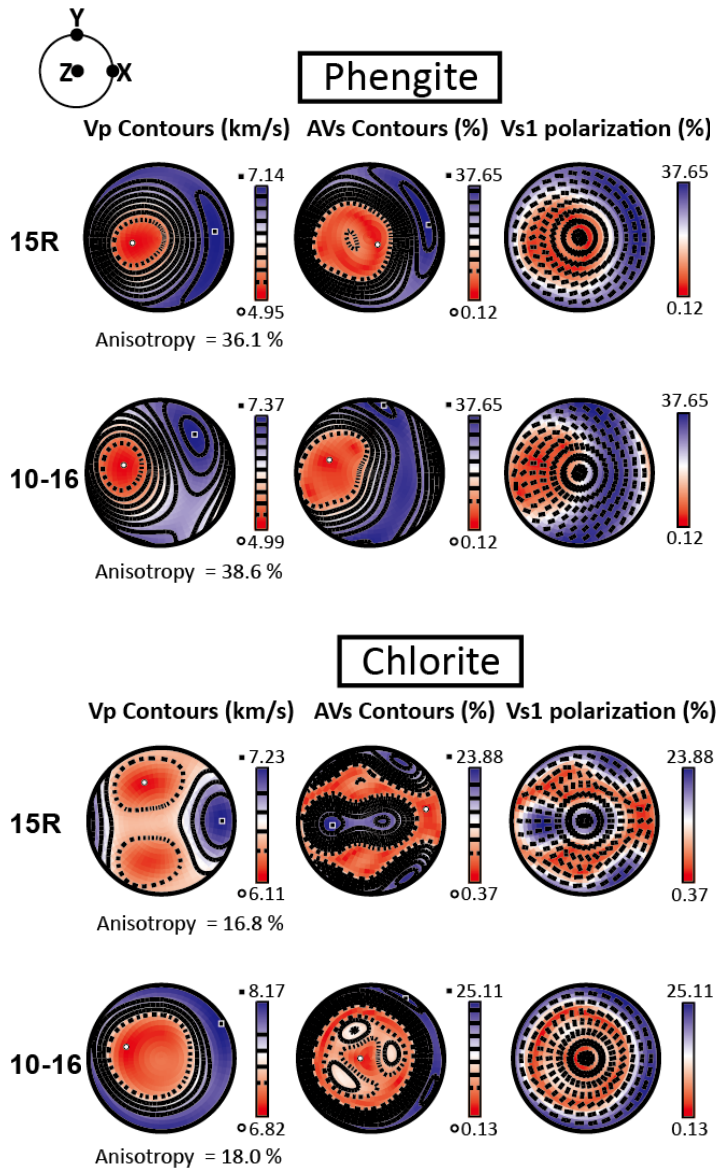


Figure 6 (a) P–wave velocity, S–wave anisotropy, and the polarization directions of the fast S–wave of phengite and chlorite in the two samples 15R and 10–16 at ambient pressure. The calculation is conducted assuming the zero pressure. Reference frame of pole figures is marked at top left. The X– and Z–directions represent lineation and the direction normal to the foliation, respectively.

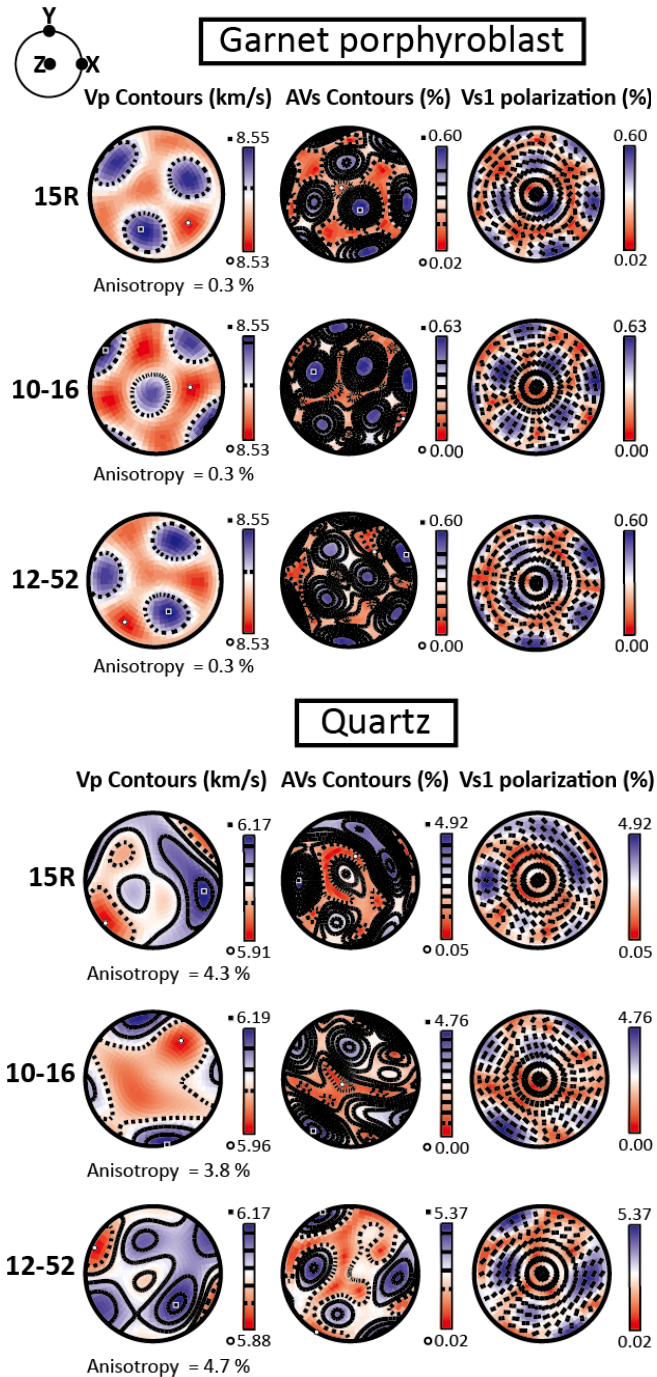


Figure 6 (b) P–wave velocity, S–wave anisotropy, and the polarization directions of the fast S–wave of garnet and quartz in the three samples at ambient pressure. Reference frame is the same as in Fig. 6a.

1.7 % for garnet and 4.9 % for quartz. Such low values may be resulted from extremely low seismic anisotropy of single crystal of garnet (Jiang, 2004) and from the very weak LPO pattern of quartz exhibited in the Grt–Cld–Tlc schist (Fig. 4c), respectively. The weak LPO patterns of quartz are may be formed because some quartz grains were probably dynamically recrystallized during subduction (Muto et al., 2011).

Seismic properties of the Grt–Cld–Tlc schist rock specimens was calculated considering the mineral mixture (talc + phengite + chlorite + garnet + quartz, which partly represents the Grt–Cld–Tlc schist), using their original modal composition and mineral LPOs (Fig. 7). Sample 10–16 with the largest amount of talc showed the highest $AV_p = 35.4$ %. Sample 12–52 which has the smallest amount of hydrous mineral (talc 28 vol. % and few or no phengite and chlorite) showed the lowest AV_p and AV_s ($AV_p = 18.3$ %, maximum $AV_s = 6.2$ %).

Seismic anisotropy of the above mineralogy composed of the five phases was also calculated as a function of volume fraction of talc (Fig. 8), to see how much the anisotropic talc contributes to whole rock seismic anisotropy comparison with phengite or chlorite. For the calculation, the deformation fabric data (LPO) of each composite mineral observed in the sample 15R was considered. Figure 8 illustrates the change of seismic anisotropy of the mineral mixture as a function of modal proportion of hydrous layered

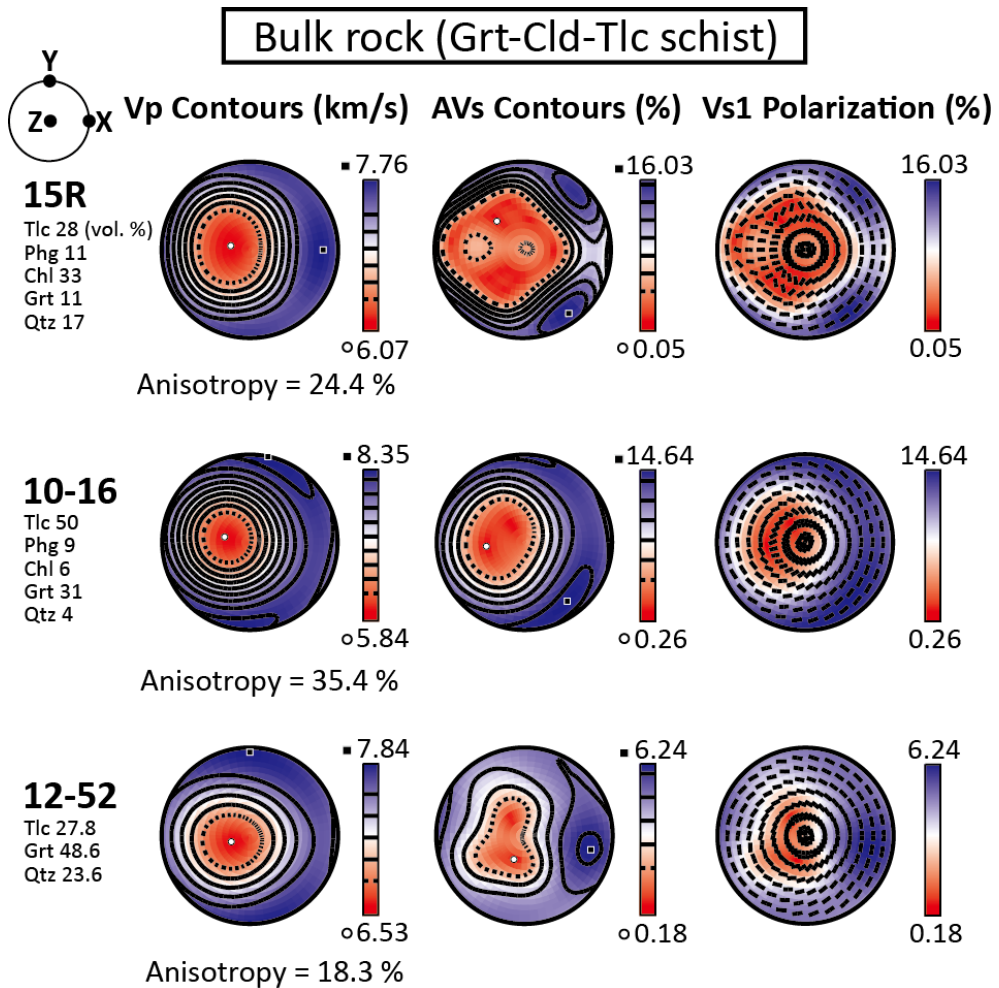


Figure 7. Seismic velocities and anisotropy from the mixture of composite minerals (talc, phengite, chlorite, garnet and quartz) in the three Grt–Cld–Tlc schist samples. Chloritoid was excluded from the mineral contents because of the lack of studied elastic parameters, and other minor/accessory phases (rutile, apatite) were also ignored. Each volume fraction (vol. %) which was re-evaluated on the base of the modal composition (Table 1) is marked at the left column.

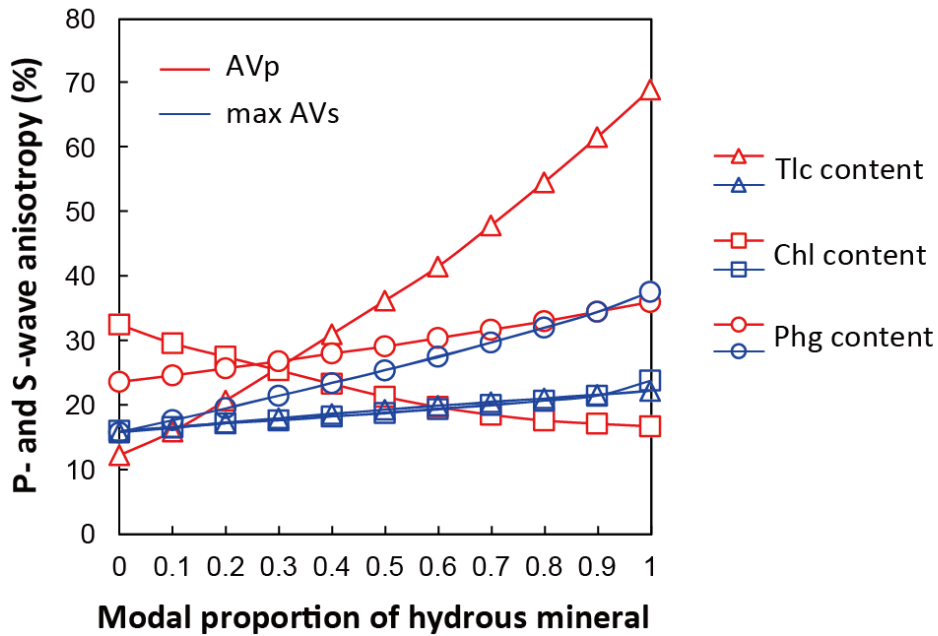


Figure 8. Relationship of hydrous mineral content and seismic anisotropy of the Grt–Cld–Tlc schist. Seismic anisotropy of P–waves (AVp) and S–waves (AVs) of the mineral mixture was calculated as a function of the modal proportion of each hydrous mineral (talc, phengite, and chlorite) based on the modal percentages of the composite minerals in the sample 15R. Modal volume fraction (Table 1) and preferred orientation data (Fig. 3, 4, 5) of the sample 15R were used for the calculation. Bulk rock composition of talc + phengite + chlorite + garnet + quartz was considered (modal fraction of chloritoid was not considered in this study). Compositions of both minor rutile and apatite were ignored.

silicate (talc, phengite, or chlorite) in the mineral mixture. As a volume ratio of talc was increased from 0 to 1 (0–100%), the seismic anisotropy of both P–wave and S–wave through the talc–bearing mineral aggregate was increased; the AV_p of the rock is increased most significantly with increasing talc content and the maximum AVs of the rock is also increased even slightly (Fig. 8).

The exclusion of chloritoid from the modal fraction to calculate the seismic anisotropy of the Grt–Cld–Tlc schist, is because there is no elastic constant data about chloritoid. Therefore, the interpretation about the above results must be carefully and reexamined in a future study.

6.3. Seismic anisotropy of talc at high pressures

In order to examine the seismic anisotropy of talc at high pressure, the single–crystal elastic stiffness constant was approximately determined at the four pressure conditions by using a trend curve for an elastic tensor using the previous calculation from Mainprice et al. (2008). The occurrence of talc could be up to the pressure relevant to the mantle wedge (0.9 GPa), peak metamorphic pressure of the Grt–Cld–Tlc schist of the Makbal Complex (2.9 GPa), and the upper pressure limit of talc stability (5.0 GPa).

Upon compression, the anisotropy of compressional wave and shear wave and the fast shear polarization were calculated, and they were plotted for talc aggregates within the Grt–Cld–Tlc schist from the Makbal UHP Complex (Fig. 9). The AVp was decreased from 68.1–69.1 % at 0 GPa to 55.2–55.9 % at 0.9 GPa, to 36.3–36.7 % at 2.9 GPa, and finally to 29.9–30.3 % at 5.0 GPa. With the same interval of pressure, the maximum AVs was also decreased in a range from 21.0–23.0 % at 0 GPa to 16.1–18.7 % at 0.9 GPa, to 13.5–17.5 % at 2.9 GPa, and finally to 9.5–13.5 % at 5.0 GPa. The direction of vertical shear polarization penetrating through talc aggregates was also estimated for a given pressure and plotted (the third columns in Figs 5, 9). For the pressure of 0 GPa (Fig. 5) and 0.9 GPa (Fig. 9a), the shear polarization anisotropy of talc was normal to shear direction (normal to the X–direction) in all three schist samples. However, for the pressure of 2.9 GPa (Fig. 9b) and 5.0 GPa (Fig. 9c), the shear polarization anisotropy of talc in the sample 15R and 10–16 was changed to being parallel to shear direction. In contrast, the polarization direction of the sample 12–52 of which LPO showed different patterns of axes of [100] and [010] from the LPOs of the other two samples (15R, 10–16) (Fig. 3) remained normal to shear direction. The S–wave polarization anisotropy is strongly dependent on the AVs distribution along the propagating direction through mineral aggregates, so the LPO of talc aggregate at high pressure should be considered as important factor (see Section 7.2).

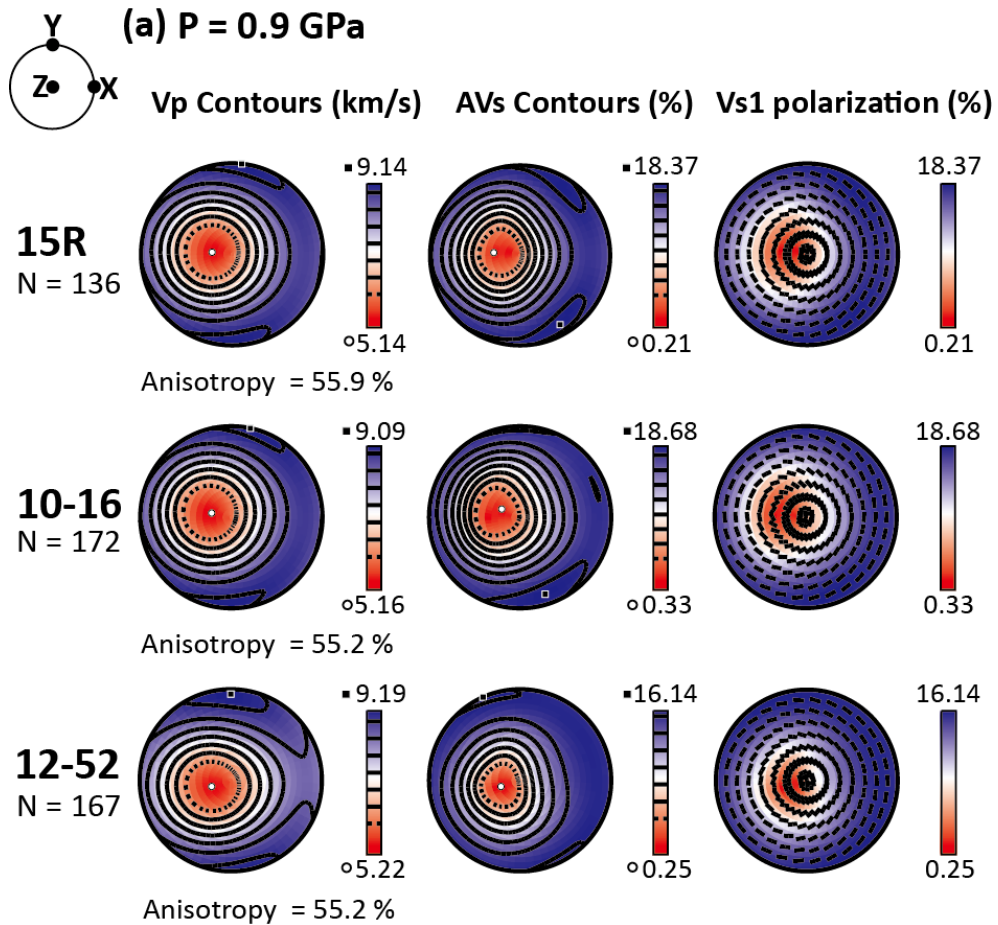


Figure 9. (a–c) P–wave velocity, S–wave anisotropy, and the polarization directions (black lines) of the fast S–wave of talc with the elastic constants for the pressure (a) 0.9 GPa, (b) 2.9 GPa, (c) 5.0 GPa. Elastic constants, crystal structure parameters, and density for each pressure were approximately calculated using the data from Mainprice et al. (2008). The X– and Z–directions represent lineation and the direction normal to the foliation, respectively. (a) Seismic velocity and anisotropy at $P = 0.9$ GPa, the representative pressure of talc occurrence in subduction zone.

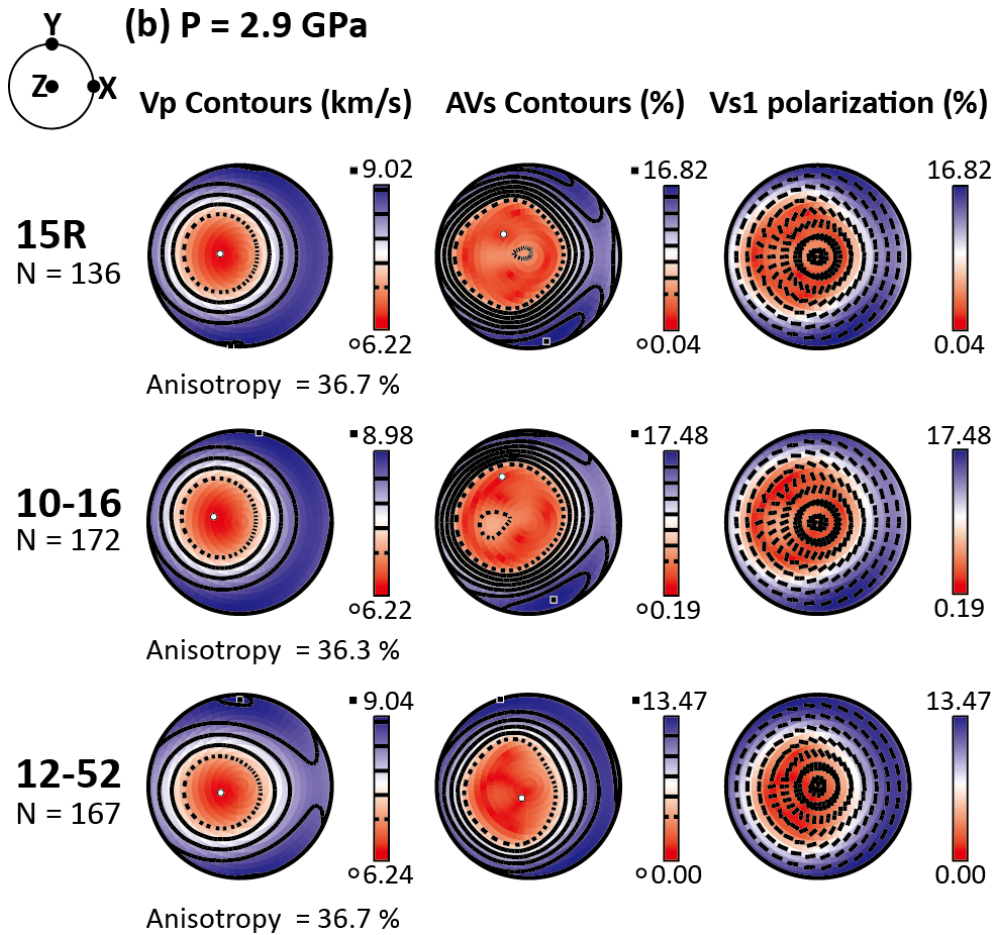


Figure 9. *Continued.* (b) Seismic velocity and anisotropy at $P = 2.9$ GPa which is similar to the peak metamorphic pressure of the Makbal Grt-Cld-Tlc schist (Meyer et al., 2014). Reference frame is the same as in Fig. 9a.

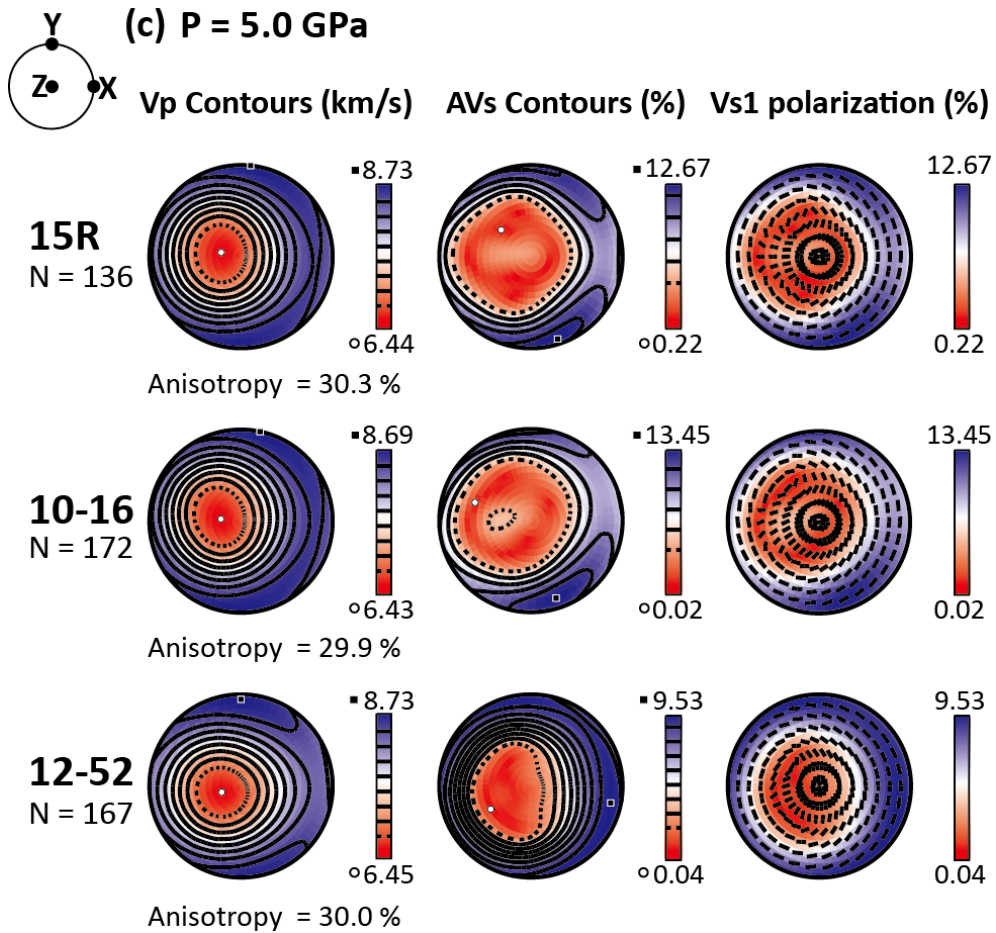


Figure 9. *Continued.* (c) Seismic velocity and anisotropy at P = 5.0 GPa which is the pressure reported as the maximum depth condition of the stability field for talc-bearing metamorphic rocks (Pawley and Wood, 1995). Reference frame is the same as in Fig. 9a.

Chapter 7. Discussion

7.1. LPO of talc in subduction zone

The measurement of talc LPO has not been done, even though some deformation experiments and natural talc-bearing schists of high strain crystal textures were previously reported. To determine the reliable contribution of hydrous minerals to the seismic anisotropy of subduction zone, natural mineral LPO should be considered. LPO of [001] axes of talc in the Grt-Cld-Tlc schist from the Makbal UHP Complex strongly distributed subnormal to the foliation, with the LPO of either [100] axes or [010] axes subnormal to the lineation (Fig. 3). Basically, it is likely that talc LPO can be easily developed in the regions of intense shear due to its platy habit and simple shear may be dominant in a subduction channel or interplate megathrusts.

In the hydrated mantle wedge, talc is closely associated with serpentine minerals. Even in serpentine rich zone at the fore-arc mantle, some amount of talc can be formed due to excess silica rich fluids released from the sinking slab. Moving further away from the trench, serpentine rich fore-arc mantle wedge is likely to be replaced by a zone of serpentine, olivine and talc by prograde breakdown of antigorite. Both two slip systems of antigorite, (001)[010] and (001)[100] are activated by its topotactic growth

after olivine during a deformation event (Bezacier et al., 2010; Brownlee et al., 2013; Jung, 2011), which show [001] axes aligned (sub)normal to the foliation or shear plane. Because crystal structure and physical properties of talc are similar to serpentine, (001) planes of antigorite and talc are probably parallel or subparallel to the mantle flow direction together (Mookherjee and Capitani, 2011). Therefore, in the context of serpentinized mantle wedge, the preferential alignment of [100] and [010] axes of talc might be correlated to the slip system of antigorite and olivine.

7.2. Seismic anisotropy of polycrystalline talc

7.2.1. Effect of LPO of talc on seismic anisotropy

In this study, seismic anisotropy of talc aggregate was calculated at the room pressure using its LPO acquired from the Grt–Cld–Tlc schists (Fig. 3), and the results are shown in the second column of Table 2 and Fig. 5. Talc shows exceptionally high P–wave anisotropy relative to the other major phyllosilicates in the Grt–Cld–Tlc schist, and the maximum shear wave anisotropy is also high (Table 2). Seismic properties of single–crystal talc are closely related to the effect of talc LPO on seismic anisotropy. As shown in Figure 10, the elastic anisotropy of talc single crystal is characterized by the slowest P–wave velocities along the [001]

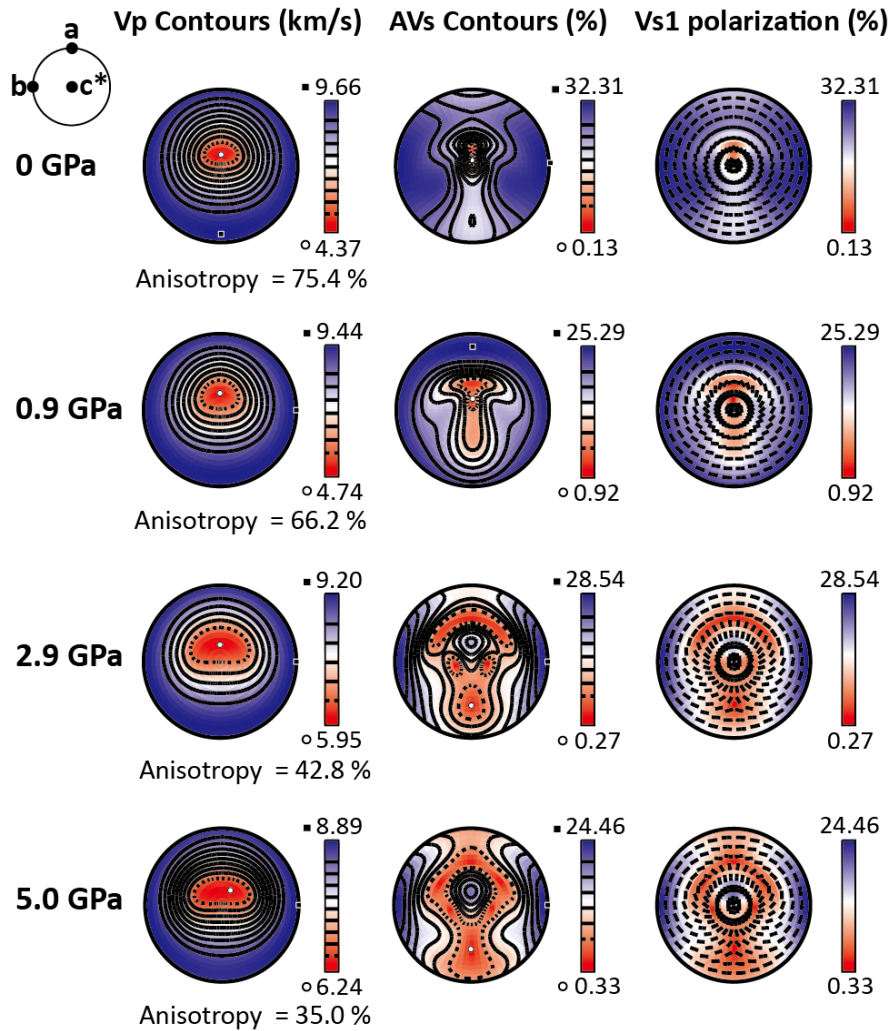


Figure 10. Single crystal P–wave velocity, S–wave maximum anisotropy, and the polarization directions (black lines) of the fast S–wave of monoclinic talc were calculated with increasing pressure. Elastic constants, crystal structure parameters, and density of talc were calculated using the data from Mainprice et al. (2008). Seismic velocity and anisotropy are presented in equal–area and upper hemisphere projections with orthogonal axes $X1 = a-$, $X2 = b-$, and $X3$ orthogonal to the $X1-X2$ plane = $c-$ axis.

Table 2. Seismic anisotropy result for each composite mineral and whole rock composition of the three Grt–Cld–Tlc schist samples. Chloritoid was excluded from the whole rock modal composition, because of the lack of elastic stiffness tensor data. Minor rutile and accessory apatite were also ignored.

Sample	AVp (%)					
	Tlc	Phg	Chl	Grt	Qtz	Whole
15R	69.1	36.1	16.8	0.3	4.3	24.4
10-16	68.7	38.6	23.5	0.3	3.8	35.4
12-52	68.1	-	-	0.3	4.7	18.3

Sample	Maximum AVs (%)					
	Tlc	Phg	Chl	Grt	Qtz	Whole
15R	22.26	37.67	23.88	0.60	4.92	16.03
10-16	23.05	32.69	38.00	0.63	4.76	14.64
12-52	21.03	-	-	0.60	5.37	6.24

axes and by similar moderate velocities along the [100] and [010] axes. Therefore, the orientation of particularly slow [001] axes tends to have first-order control over the seismic anisotropy pattern of polycrystalline talc. This tendency is also consistent with serpentine minerals which [001] axes are aligned subnormal to shear plane at tectonic shear zone (Bezacier et al., 2010; Boudier et al., 2010; Brownlee et al., 2013; Mookherjee and Capitani, 2011; Watanabe et al., 2014).

Even though the LPO of talc aggregate has an effect of reducing the intrinsic seismic anisotropy of single-crystal talc, the polycrystalline talc showed still high seismic anisotropy in this study likely due to the strong LPO of [001] axes (Table 3). It was previously reported that the anisotropy of deformed monomineral aggregate is lower than that of the constituent single crystal, and often it would be a factor of 2–3 smaller depending on the degree of alignment and the detailed texture (Karki et al., 2001; Mainprice et al., 2000). It might be because not all mineral grains can have the LPO perfectly parallel to the foliation under the shear deformation event in general. However, when the seismic anisotropy of talc aggregates in the Grt–Cld–Tlc schist ($AV_p = 68.1\text{--}69.1\%$, maximum $AV_s = 23.0\%$) is compared to that of talc single crystal ($AV_p = 75.4\%$, maximum $AV_s = 32.3\%$; Figure 10, Table 3), the seismic anisotropy about polycrystalline talc at zero pressure are a factor of 1.1–1.54 lower than that of single-crystal talc and

Table 3. Calculated seismic anisotropy of talc using the pressure-dependent elastic constant and the LPO of talc measured in each Grt–Cld–Tlc sample.

Sample	Grt-Cld-Tlc schist (this study)			Single-crystal talc ^a
	15R	10-16	12-52	
Pressure (GPa)	AVp (%) of talc			
0	69.1	68.7	68.1	75.4
0.9	55.9	55.2	55.2	66.2
2.9	36.7	36.3	36.7	42.8
5.0	30.3	29.9	30.0	35.0

Sample	Grt-Cld-Tlc schist			Single-crystal talc
	15R	10-16	12-52	
Pressure (GPa)	max. AVs (%) of talc			
0	22.26	23.05	21.03	32.31
0.9	18.37	18.68	16.14	25.29
2.9	16.89	17.48	13.47	28.54
5.0	12.67	13.45	9.53	24.46

^aFor comparison, the single-crystal seismic anisotropy of talc with crystal-preferred orientation is also tabulated. The consistent pole figure data of single-crystal talc is also illustrated in Figure 10.

especially for AVp, the reduction ratio is about 1.1 (Table 3). The smaller reduction ratio than the expected might be caused by the strong LPO of talc [001] axes developed in the studied samples, as well as its extremely anisotropic behavior which is distinguished from other major materials in the earth's mantle like olivine, pyroxene, etc. (Mainprice et al., 2000; Mainprice and Ildefonse, 2009). In addition, seeing Figure 8, the volume fraction of anisotropic talc also influenced seismic anisotropy of bulk talc-bearing metamorphic rock. Therefore, it is suggested that the impact of talc on seismic anisotropy would depend on its volume percentage and their degree of LPO.

The apparent difference between the talc LPOs of three schist samples is the distribution pattern of [110], [100], and (010) crystallographic axes. For the sample 12-52, the [100] axes (corresponding to a-axis of talc) show the maximum concentration subnormal to the lineation in the foliation plane and the (010) poles (b-axis of talc) subparallel to the foliation. On the other hand, both samples 15R and 10-16 show similar LPOs in that [100] axes preferentially distribute subparallel to the lineation and (010) poles subnormal to the lineation in the foliation (Fig. 3). The difference in the degree of seismic anisotropy between the studied samples at zero pressure is just about 1.7 % in AVp and 2.0 % in maximum AVs. This discrepancy may infer that the effect of the talc LPO of [110] axes, [100] axes and (010) poles on seismic anisotropy is less important than that of the talc LPO of weak (001) basal plane.

One can easily expect that preferred orientation of [001] axes normal to foliation is prevalent in other layered silicates (Dempsey et al., 2011; Padrón-Navarta et al., 2012; Wenk et al., 2010). However, the way how talc LPOs of the other two major crystallographic axes [100] and (010) are distributed would be important to the polarization direction of the fast S-wave at high pressure (Section 7.2.2).

7.2.2. Effect of pressure on seismic anisotropy of talc

Seismic anisotropy of polycrystalline talc was also calculated using pressure-dependent elastic constants for the pressures of 0.9, 2.9, and 5 GPa (Fig. 9, Table 3). The magnitude of the anisotropy for P-wave and S-wave are plotted in Fig. 11. The significant decrease of the seismic anisotropy of polycrystalline talc was shown as pressure increases up to 5 GPa (Fig. 11). It means that the compressed talc crystals present in the deep slab would exhibit much small seismic anisotropy, even if they might be preferentially aligned (sub)parallel to the subduction channel flow or mantle flow over the slab. It is assumed that most of the talc grains in the aggregates are compressed by the same way depending on the elastic stiffness tensors, crystal axes parameters, and density at the given pressure conditions. It may be doubtful that all talc grains follow the modelled compressional behavior, but the decreasing trend of seismic anisotropy as a function of pressure

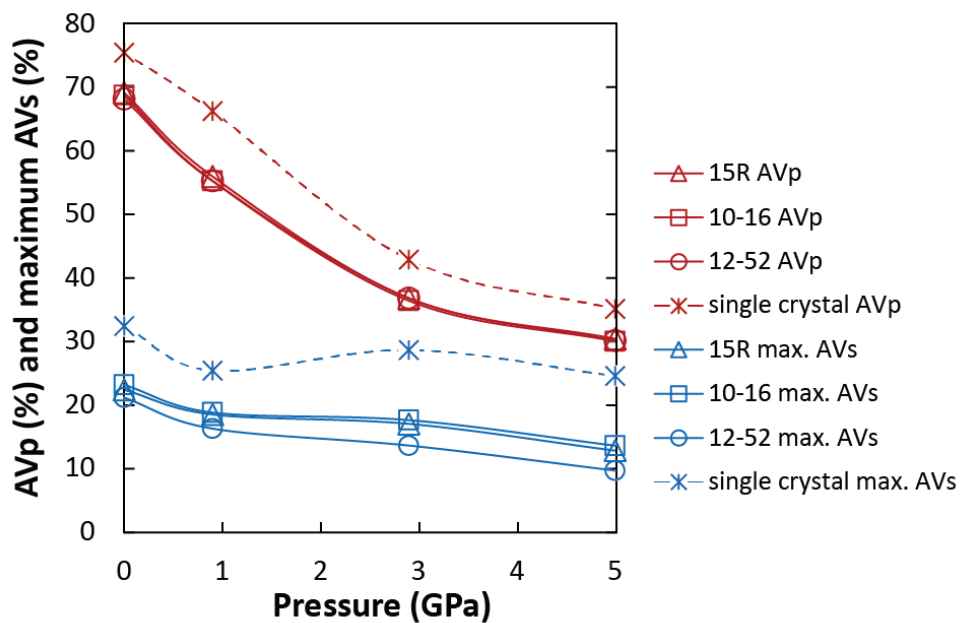


Figure 11. Plot of seismic anisotropy of polycrystalline talc in the Grt-Cld-Tlc schists (sample 15R, 10-16, 12-52) and single-crystal talc as a function of pressure. Seismic anisotropies of talc decreased as pressure increased, and the anisotropies of polycrystal were lower than that of single crystal.

will be apparent to a certain degree.

Our results of AVs of talc at high pressures showed the higher magnitudes than that of olivine in the previous studies. According to the previous experimental studies, the maximum AVs of B-type olivine are 4.3 % at 1.9 GPa (Ohuchi et al., 2015), 6.9–7.9 % at 2.1 GPa and 7.4 % at 3 GPa (Ohuchi et al., 2012), and 2.7 % at 3.1 GPa and 2.3 % at 3.6 GPa (Jung et al., 2009). However, for talc, the maximum S-wave anisotropies were calculated as 13.5–17.5 % at 2.9 GPa and 9.5–13.5 % at 5.0 GPa (Table 3). All of them are much higher than the magnitude of AVs of olivine at overall high-pressure conditions. Therefore, talc is still able to act as an anisotropic medium in the olivine-rich mantle wedge at high pressures.

Both the AVp and the maximum AVs of polycrystalline talc are lower than those of single-crystal talc. The seismic anisotropy of the polycrystalline talc continuously decreased in response to pressure increase even though there is a slight increase of single-crystal shear wave anisotropy of talc in the short pressure range 1–2 GPa (Fig. 11). It might be relevant to the auxetic behavior (negative Poisson's ratio; tendency to flatten on expansion) of talc at low pressure (Mainprice et al., 2008). The decreasing tendency in seismic anisotropy of single crystal as pressure increases has also been found in talc (Mainprice et al., 2008), serpentine antigorite (Mookherjee and Capitani, 2011), chlorite (Mookherjee

and Mainprice, 2014), and also phlogopite mica (Chheda et al., 2014), although the alignment of only weak basal plane (001) normal to the foliation was taken into account for calculating their anisotropic elasticity.

The shear direction at a subduction zone could be associated with the mantle flow, subducting direction of oceanic slab, or dip direction of faults in oceanic crust. Therefore, the shear wave polarization direction could also be described related to trench. The polarization direction of vertically propagating fast-shear wave through talc varied from trench-parallel to trench-normal at high pressure of 2.9 GPa and 5.0 GPa in the samples 15R and 10-16, but in the sample 12-52, the polarization direction was still trench-parallel during pressure increases to 5 GPa (Fig. 12). This change was ascribed to the elastic properties of talc single crystal at high pressure and the different fabrics of talc in the three samples. As shown in Figure 10, the shear wave seismic anisotropy of talc a-axis ([100] axes) is lower than that of talc b-axis ([010] axes), and also one can find the higher AVs along c-axis ([001] axes) of talc at high pressure (2.9 GPa, 5.0 GPa). Note that the polarization direction of vertically propagating fast-shear wave through the single-crystal talc is rotated about 90° at the pressure 2.9 GPa. It implies that LPO pattern of a- and b-axis could have critical control over the polarization direction of fast S-wave penetrating talc layer present at high/ultrahigh pressure.

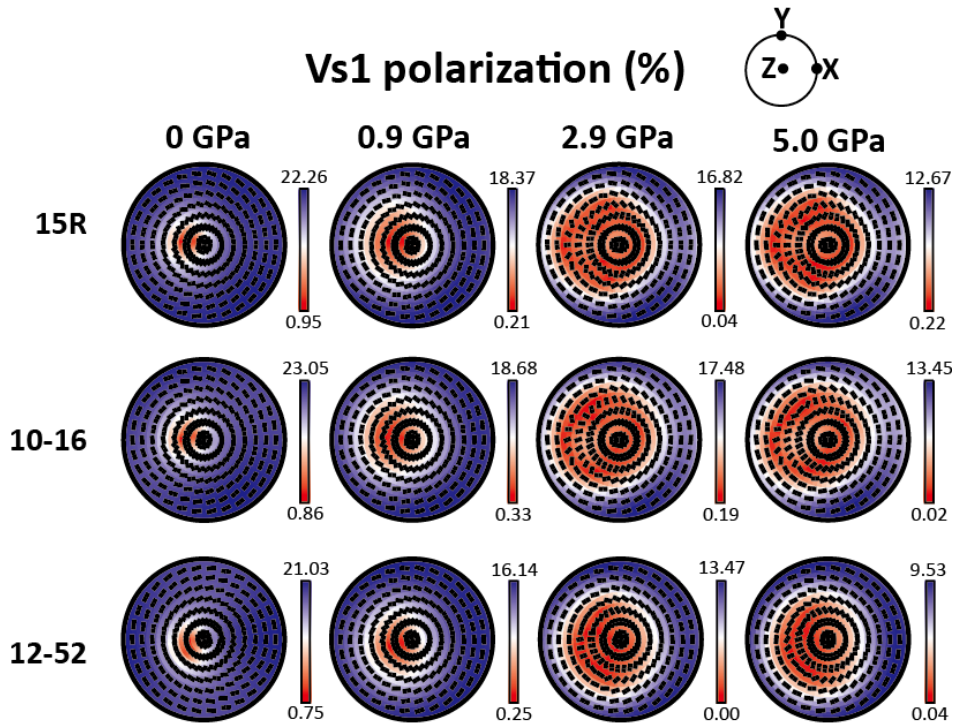


Figure 12. Variation on the polarization directions of fast S–wave as a function of the given pressures. The rotation of $\approx 90^\circ$ of the polarization planes of vertically penetrating fast S–wave occurs in the two talc aggregates (15R and 10–16) of which LPO of talc [100] axes align subparallel to the schist lineation (L), at the pressure of 2.9 GPa. Such variation is not observed in the sample 12–52 which exhibits LPOs of talc (010) poles subparallel to the lineation. The X–direction is parallel to the lineation and the Z–direction normal to the foliation (S). The colour bar on the right indicates the degree of shear wave anisotropy (%).

The relationship between the LPO pattern of those two crystallographic axes and the polarization direction of fast S-wave at the given high pressures is illustrated in Figure 12. Our data demonstrated that LPO of talc crystals could affect to the pattern of AVs propagating polycrystalline talc and the polarization direction of vertically propagating fast-shear wave (trench-parallel or trench-normal) at high/ultrahigh pressure of 2.9–5.0 GPa. Because the AVs propagating the a-axes and that penetrating the b-axes is different (Fig. 10), the dominant LPO of those two axes could influence the bulk AVs of talc aggregate and also the polarization direction of shear wave (Fig. 12). As hydrated oceanic slab is subducted to the depth of eclogite-facies and becomes talc-bearing system, the distribution of [100] axes and (010) poles (rather than its weak [001] basal planes) of large amount of talc could change the polarization of vertically propagating shear wave from the trench-parallel anisotropy to the trench-normal anisotropy moving from fore-arc to back-arc areas.

B-type olivine LPO has been also suggested to be formed in the mantle wedge and to influence trench-parallel seismic anisotropy observed at forearc region (Jung and Karato, 2001; Jung et al., 2009; Katayama and Karato, 2006). However, the trench-parallel anisotropy with the long delay time in some subduction zones (e.g. 1–2 sec in the Ryukyu arc; Long and Hilst, 2006) was hard to be explained by only 100% of B-type olivine LPO.

Therefore, the long delay time would be caused by more anisotropic material such as talc formed in the mantle wedge. The seismic anisotropy of the strongly deformed talc is much higher than that of B-type olivine aggregate at high pressures (Fig. 13). For the condition at the pressure of $P \approx 3$ GPa, the maximum AVs of talc in the Grt-Cld-Tlc schist was 17 %. On the other hand, the maximum AVs of experimentally deformed B-type olivine was previously reported as about 3 % which is much lower than that of talc at the similar pressure of 3.1 GPa (Jung et al., 2009). We can use the equation $dt = L \times AVs / \langle Vs \rangle$ for the relationship between delay time (dt) and the thickness of anisotropic medium (L) (Silver and Chan, 1991). If we use the previously reported magnitude of AVs based on the B-type olivine (Jung et al., 2009), the anisotropic layer of olivine thickness 200–330 km was required to explain the delay time observed at the Ryukyu arc. In contrast, if we use talc LPO, much thinner anisotropic layer of talc thickness 30–50 km is needed to explain the long delay time at the Ryukyu arc even though the decreased AVs at high pressure of $P \approx 3$ GPa.

7.2.3. Effect of subducting angle on seismic anisotropy of talc

The seismic anisotropy and the polarization direction of the fast S-wave would also be varied by the change of dipping angle of subducting slab (θ). Assuming 2-dimensional corner flow for simplicity, the seismic properties of talc were calculated for $\theta =$

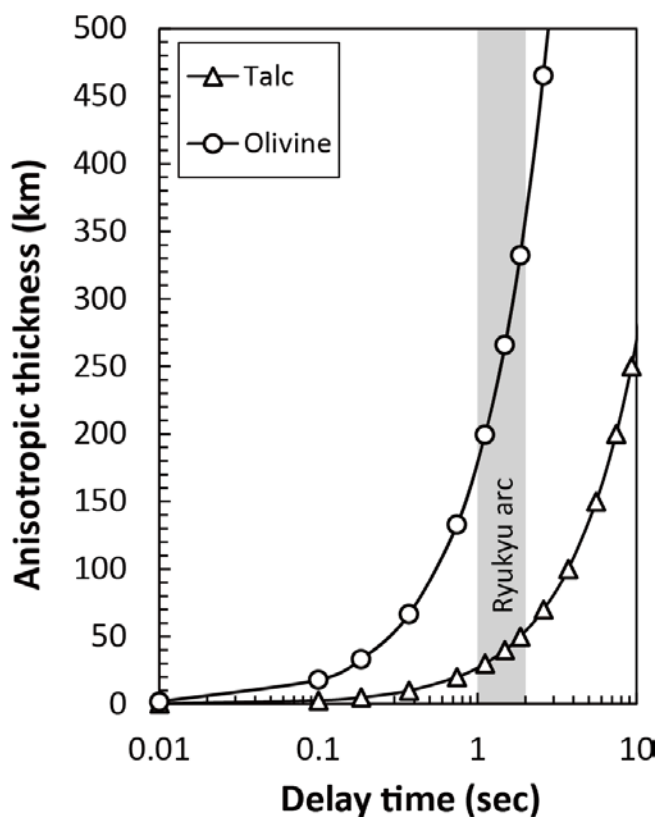


Figure 13. Anisotropic thickness of talc and olivine as a function of delay time, which was calculated the relationship $dt = L \times AVs / \langle Vs \rangle$ (Silver and Chan, 1991). For the case of talc, the $AVs = 17.5\%$ and the average shear velocity $\langle Vs \rangle = 4.7$ km/s were taken from the sample 10–16. The $AVs = 2.7\%$ and the $\langle Vs \rangle = 4.8$ km/s of B-type olivine were used which were determined by the experimental study of olivine aggregates at the high pressure of $P = 3.1$ GPa (Jung et al., 2009). When we use the above data, the long delay time (1–2 s) observed in some forearc region (e.g. Ryukyu arc) requires an anisotropic layer of olivine thickness 200–330km, but only 30–50 km talc thickness at the high pressure of 3 GPa.

0°, 30°, 45°, 60° using the LPO of the sample 10–16 and the elastic constants for the pressure 2.9 GPa (Fig. 14). Seeing the P–wave velocity contours for talc, the least seismic anisotropy of P–wave was observed near the concentration of the [001] axes subnormal to the foliation (Fig. 14). This foliation could be regarded as a plane of mantle flow overlying the subducting slab or interface between the slab and hydrated mantle wedge. When the dipping angle of slab was increased to $\theta = 30^\circ, 45^\circ, 60^\circ$, the polarization direction of the vertically propagating fast S–wave (V_{s1}) was changed to nearly parallel to Y–direction (trench–parallel anisotropy). In that propagating direction, the magnitude of AVs was increased to 4, 9, 13 %, respectively. The AVs is higher for the steeper dipping angle of talc, so the corner of mantle wedge and also the hydrated fractures in the shallow slab could be taken into account as a place of $\theta \approx 90^\circ$. For the hydrated fracture or fault zone, Faccenda et al. (2008) reported the presence of talc in the sub–vertical fault zones in ultramafic slab as a possible anisotropic source. Therefore, the talc layer in the steeply dipping slab or in the hydrated fault zone in the slab may contribute significantly to the magnitude of seismic anisotropy of vertically penetrating fast S–wave.

The higher magnitude of AVs of an anisotropic mineral corresponds to the longer delay time of shear wave splitting after propagating the anisotropic layer of the constituent mineral. To consider the effect of both pressure and dipping angle on the

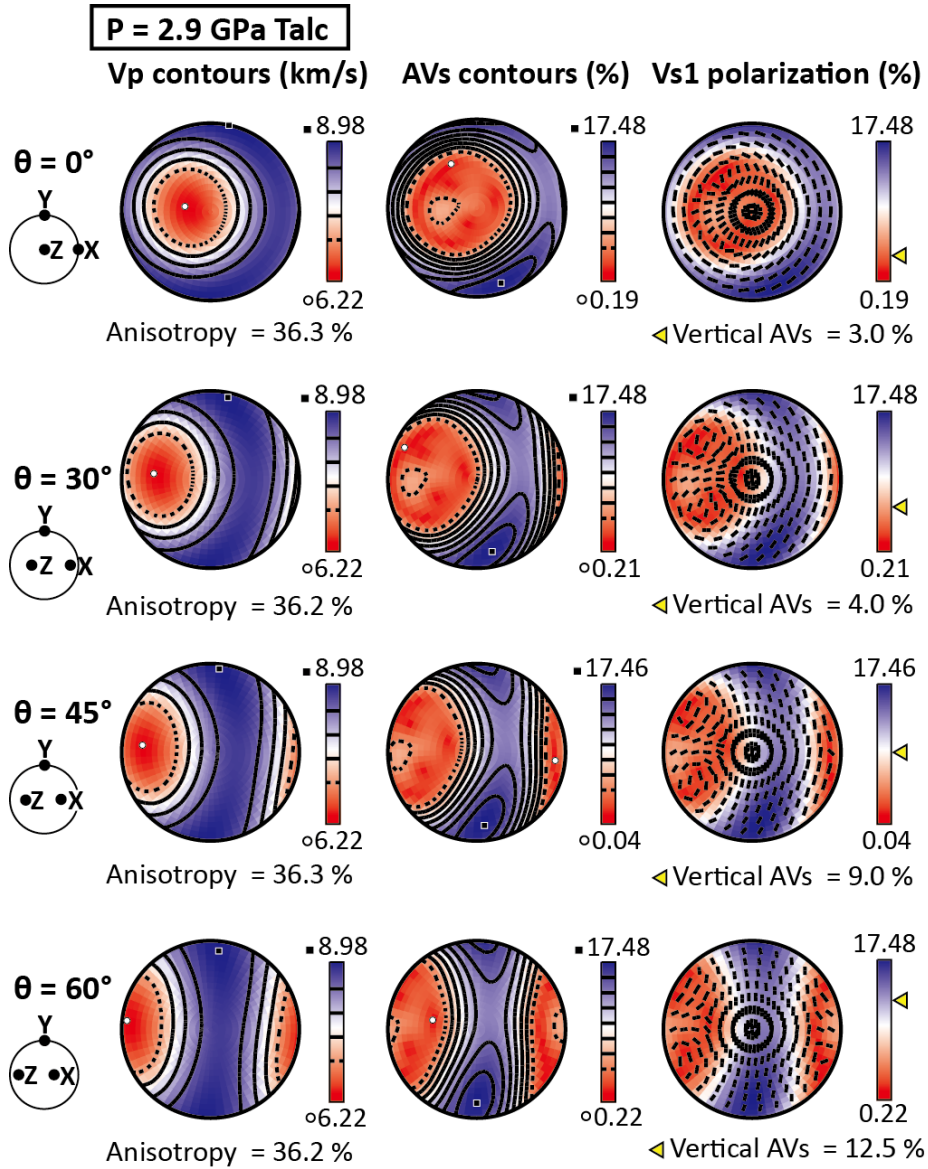


Figure 14. Seismic anisotropy of talc (sample 10–16) in response to the change of subduction dipping angle at the pressure of 2.9 GPa which is the peak metamorphic pressure of the Grt–Cld–Tlc schist sample (Meyer et al., 2014). The X–direction is parallel to the lineation which would be developed along subduction direction and the Z–direction is normal to the foliation. The vertical AVs (%) (yellow triangle arrows) means the seismic anisotropy of vertically penetrating fast S–wave.

magnitude of AVs, delay time/thickness of anisotropic layer ($dt/L = AVs/\langle Vs \rangle$) was calculated for the polycrystalline talc for some pressure conditions, as a function of dipping angle (Fig. 15). Although the compressional effect would diminish the influence of anisotropic talc, our calculations suggest that steep dipping angle of slab could increase the magnitude of shear wave anisotropy. It provides that in a lowermost mantle wedge (≈ 0.9 GPa), the presence of anisotropic talc layer about 25–40 km thick or equivalent cumulated talc thickness along a seismic ray path could possibly explain the delay time of 1 sec according to the incidence angle (Fig. 15), although the thickness must be even larger at a deeper mantle over a slab far from forearc wedge. Much less anisotropic olivine (Jung et al., 2006; Jung et al., 2009; Katayama and Karato, 2006) advocates that the LPO of strongly deformed talc can significantly influence to the wedge-derived delay time in the olivine + talc mantle. In addition, the results also imply that talc is the most important hydrous mineral to generate slab-derived anisotropies until ultra-high pressure conditions.

In the place just under the overriding plate ($\theta \approx 0^\circ$), the (001) planes of talc would likely be horizontal and parallel to the overriding plate. Depending on the LPO of [100] and [010] axes, the vertical shear wave polarization could be slightly changed and exhibit trench-parallel or trench-normal polarization at high pressure (Fig. 12). At the base of the mantle wedge, talc can be formed at the lowermost mantle wedge by excess silica rich fluids

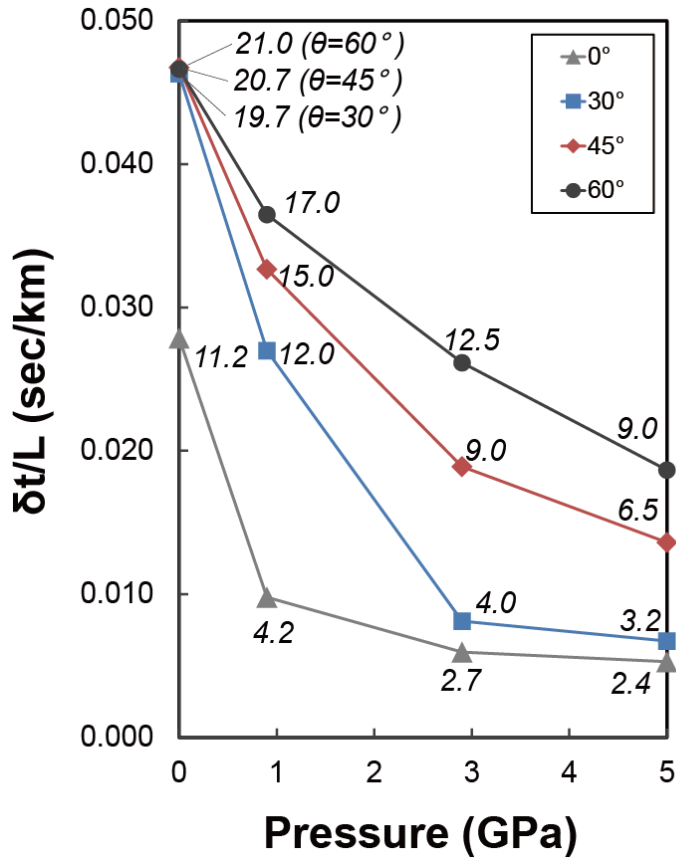


Figure 15. Delay time/thickness of anisotropic layer for the case of 100 % talc calculated as $dt/L = AV_s/\langle V_s \rangle$ which is able to be derived from Silver and Chan (1991). Magnitudes of vertical S-wave anisotropies (as percentage) of talc as a function of pressures (0, 0.9, 2.9, and 5.0 GPa) are marked on each point for the four dipping angles.

released from the dehydrated slab. The ultramafic slab would be also hydrated at a depth >100 km and talc can be present in the dipping slab. Vertically penetrating both the lowermost mantle wedge and talc-bearing slab with dipping angle $\theta \geq 30^\circ$, fast S-wave would be polarized to trench-parallel direction (Fig. 14). It is no matter how [100] axes or [010] axes of talc are preferentially aligned. It is suggested that when the talc-bearing mafic oceanic slab is subducted with steep dipping angle, talc would produce the polarization direction of the fast S-wave to be trench-parallel for receiving stations in the forearc or above the serpentized portion of mantle wedge and hydrated slab.

This effect of talc on seismic anisotropy is similar to that of other hydrous minerals present in the mantle wedge such as serpentine and chlorite which were reported by previous studies (Jung, 2011; Katayama et al., 2009; Kim and Jung, 2015). In addition, other constituent minerals composing hydrated oceanic slab could also affect to the trench-parallel anisotropy of blueschist and eclogite depending on the mineral LPO of glaucophane and lawsonite, and also depending on the dipping angle of the mafic oceanic slab (Cao and Jung, 2016; Cao et al., 2013, 2014).

Chapter 8. Conclusion

We studied the Grt–Cld–Tlc schist in the Makbal UHP Complex to examine the LPO of polycrystalline talc. We found that the LPO of talc which shows maximum concentration of [001] axes subnormal to the foliation would mostly control the seismic anisotropies of polycrystalline talc. The concentration of [100] axes and (010) poles of talc parallel to the foliation also could contribute to the magnitude and the geometry of shear wave anisotropies. Seismic anisotropy of talc was remarkably high: 68–69 % for P–wave and 21–23 % for S–wave. When the pressure–dependent elastic constants were applied in the calculation of seismic properties of talc, the magnitude of vertically propagating shear wave anisotropy of talc became lower under the higher pressure conditions, but talc still could act as an anisotropic medium when the dipping angle of subducting slab is steeper than 45 degrees. Therefore, the LPO of talc could affect to strong trench–parallel seismic anisotropy of vertically penetrating fast shear wave at the intraplates in subduction zones with a steep dipping angle.

References

- Alexeiev, D. V., Ryazantsev, A. V., Kröner, A., Tretyakov, A. A., Xia, X., and Liu, D. Y., 2011, Geochemical data and zircon ages for rocks in a high-pressure belt of Chu–Yili Mountains, southern Kazakhstan: Implications for the earliest stages of accretion in Kazakhstan and the Tianshan: *Journal of Asian Earth Sciences*, v. 42, no. 5, p. 805–820.
- Allen, M., Windley, B., and Zhang, C., 1993, Palaeozoic collisional tectonics and magmatism of the Chinese Tien Shan, central Asia: *Tectonophysics*, v. 220, no. 1, p. 89–115.
- Bach, W., Garrido, C. J., Paulick, H., Harvey, J., and Rosner, M., 2004, Seawater-peridotite interactions: First insights from ODP Leg 209, MAR 15 N: *Geochemistry, Geophysics, Geosystems*, v. 5, no. 9.
- Bailey, E., and Holloway, J. R., 2000, Experimental determination of elastic properties of talc to 800 C, 0.5 GPa; calculations of the effect on hydrated peridotite, and implications for cold subduction zones: *Earth and Planetary Science Letters*, v. 183, no. 3, p. 487–498.
- Beaumont, C., Jamieson, R. A., Butler, J., and Warren, C., 2009, Crustal structure: a key constraint on the mechanism of ultra-high-pressure rock exhumation: *Earth and Planetary Science Letters*, v. 287, no. 1, p. 116–129.

- Bezacier, L., Reynard, B., Bass, J. D., Sanchez-Valle, C., and Van de Moortèle, B., 2010, Elasticity of antigorite, seismic detection of serpentinites, and anisotropy in subduction zones: *Earth and Planetary Science Letters*, v. 289, no. 1, p. 198–208.
- Birch, F., 1978, Finite strain isotherm and velocities for single-crystal and polycrystalline NaCl at high pressures and 300° K: *Journal of Geophysical Research: Solid Earth (1978–2012)*, v. 83, no. B3, p. 1257–1268.
- Boschi, C., Früh-Green, G. L., and Escartín, J., 2006, Occurrence and significance of serpentinite-hosted, talc- and amphibole-rich fault rocks in modern oceanic settings and ophiolite complexes: an overview: *Ofioliti*, v. 31, no. 2, p. 129–140.
- Boudier, F., Baronnet, A., and Mainprice, D., 2010, Serpentine mineral replacements of natural olivine and their seismic implications: oceanic lizardite versus subduction-related antigorite: *Journal of Petrology*, v. 51, no. 1–2, p. 495–512.
- Brownlee, S. J., Hacker, B. R., Harlow, G. E., and Seward, G., 2013, Seismic signatures of a hydrated mantle wedge from antigorite crystal-preferred orientation (CPO): *Earth and Planetary Science Letters*, v. 375, p. 395–407.
- Cao, Y., and Jung, H., 2016, Seismic properties of subducting oceanic crust: Constraints from natural lawsonite-bearing blueschist and eclogite in Sivrihisar Massif, Turkey:

Physics of the Earth and Planetary Interiors, v. 250, p. 12–30.

Cao, Y., Jung, H., and Song, S., 2013, Petro-fabrics and seismic properties of blueschist and eclogite in the North Qilian suture zone, NW China: Implications for the low-velocity upper layer in subducting slab, trench-parallel seismic anisotropy, and eclogite detectability in the subduction zone.: *Journal of Geophysical Research: Solid Earth*, v. 118, no. 6, p. 3037–3058.

Cao, Y., Jung, H., and Song, S., 2014, Microstructures and petro-fabrics of lawsonite blueschist in the North Qilian suture zone, NW China: Implications for seismic anisotropy of subducting oceanic crust: *Tectonophysics*, v. 628, p. 140–157.

Chen, Y., Ye, K., Wu, T., and Guo, S., 2013, Exhumation of oceanic eclogites: thermodynamic constraints on pressure, temperature, bulk composition and density: *Journal of Metamorphic Geology*, v. 31, no. 5, p. 549–570.

Chheda, T. D., Mookherjee, M., Mainprice, D., dos Santos, A. M., Molaison, J. J., Chantel, J., Manthilake, G., and Bassett, W. A., 2014, Structure and elasticity of phlogopite under compression: Geophysical implications: *Physics of the Earth and Planetary Interiors*, v. 233, p. 1–12.

Connolly, J. A. D., and Kerrick, D. M., 2002, Metamorphic controls on seismic velocity of subducted oceanic crust at 100–

- 250 km depth: *Earth and Planetary Science Letters*, v. 204, no. 1–2, p. 61–74.
- Dempsey, E. D., Prior, D. J., Mariani, E., Toy, V. G., and Tatham, D. J., 2011, Mica-controlled anisotropy within mid-to-upper crustal mylonites: an EBSD study of mica fabrics in the Alpine Fault Zone, New Zealand: Geological Society, London, Special Publications, v. 360, no. 1, p. 33–47.
- Escartín, J., Mével, C., MacLeod, C., and McCaig, A., 2003, Constraints on deformation conditions and the origin of oceanic detachments: The Mid-Atlantic Ridge core complex at 15° 45' N: *Geochemistry, Geophysics, Geosystems*, v. 4, no. 8.
- Escartín, J., Andreani, M., Hirth, G., and Evans, B., 2008, Relationships between the microstructural evolution and the rheology of talc at elevated pressures and temperatures: *Earth and Planetary Science Letters*, v. 268, no. 3–4, p. 463–475.
- Faccenda, M., Burlini, L., Gerya, T. V., and Mainprice, D., 2008, Fault-induced seismic anisotropy by hydration in subducting oceanic plates: *Nature*, v. 455, no. 7216, p. 1097–1100.
- Gerya, T. V., Stöckhert, B., and Perchuk, A. L., 2002, Exhumation of high-pressure metamorphic rocks in a subduction channel: A numerical simulation: *Tectonics*, v. 21, no. 6, p. 6–1–6–19.

- Ghent, E., Tinkham, D., and Marr, R., 2009, Lawsonite eclogites from the Pinchi Lake area, British Columbia—new P–T estimates and interpretation: *Lithos*, v. 109, no. 3–4, p. 248–253.
- Gilligan, A., Roecker, S. W., Priestley, K. F., and Nunn, C., 2014, Shear velocity model for the Kyrgyz Tien Shan from joint inversion of receiver function and surface wave data: *Geophysical Journal International*, v. 199, no. 1, p. 480–498.
- Godfrey, N. J., Christensen, N. I., and Okaya, D. A., 2000, Anisotropy of schists: contribution of crustal anisotropy to active source seismic experiments and shear wave splitting observations: *Journal of Geophysical Research: Solid Earth*, v. 105, no. B12, p. 27991–28007.
- Guillot, S., Hattori, K., Agard, P., Schwartz, S., and Vidal, O., 2009, Exhumation processes in oceanic and continental subduction contexts: a review, *Subduction zone geodynamics*, Springer, p. 175–205.
- Hacker, B. R., Abers, G. A., and Peacock, S. M., 2003, Subduction factory 1. Theoretical mineralogy, densities, seismic wave speeds, and H₂O contents: *Journal of Geophysical Research*, v. 108, no. B1.
- Haerinck, T., Wenk, H.–R., Debacker, T. N., and Sintubin, M., 2015, Preferred mineral orientation of a chloritoid-bearing slate in relation to its magnetic fabric: *Journal of Structural Geology*, v. 71, p. 125–135.

- Hirauchi, K. i., den Hartog, S. A. M., and Spiers, C. J., 2012, Weakening of the slab–mantle wedge interface induced by metasomatic growth of talc: *Geology*, v. 41, no. 1, p. 75–78.
- Jiang, F., 2004, Single–crystal elasticity of grossular– and almandine–rich garnets to 11 GPa by Brillouin scattering: *Journal of Geophysical Research*, v. 109, no. B10.
- Jung, H., 2011, Seismic anisotropy produced by serpentine in mantle wedge: *Earth and Planetary Science Letters*, v. 307, no. 3, p. 535–543.
- Jung, H., and Karato, S.–i., 2001, Water–induced fabric transitions in olivine: *Science*, v. 293, no. 5534, p. 1460–1463.
- Jung, H., Katayama, I., Jiang, Z., Hiraga, T., and Karato, S.–I., 2006, Effect of water and stress on the lattice–preferred orientation of olivine: *Tectonophysics*, v. 421, no. 1, p. 1–22.
- Jung, H., Mo, W., and Green, H. W., 2009, Upper mantle seismic anisotropy resulting from pressure–induced slip transition in olivine: *Nature Geoscience*, v. 2, no. 1, p. 73–77.
- Jung, S., Jung, H., and Austrheim, H., 2014, Characterization of olivine fabrics and mylonite in the presence of fluid and implications for seismic anisotropy and shear localization: *Earth, Planets and Space*, v. 66, no. 1, p. 1–21.
- Karato, S.–i., Jung, H., Katayama, I., and Skemer, P., 2008, Geodynamic significance of seismic anisotropy of the

- upper mantle: new insights from laboratory studies: *Annu. Rev. Earth Planet. Sci.*, v. 36, p. 59–95.
- Karki, B. B., Stixrude, L., and Wentzcovitch, R. M., 2001, High-pressure elastic properties of major materials of Earth's mantle from first principles: *Reviews of Geophysics*, v. 39, no. 4, p. 507–534.
- Katayama, I., Hirauchi, K.-i., Michibayashi, K., and Ando, J.-i., 2009, Trench-parallel anisotropy produced by serpentine deformation in the hydrated mantle wedge: *Nature*, v. 461, no. 7267, p. 1114–1117.
- Katayama, I., and Karato, S.-i., 2006, Effect of temperature on the B-to C-type olivine fabric transition and implication for flow pattern in subduction zones: *Physics of the Earth and Planetary Interiors*, v. 157, no. 1, p. 33–45.
- Kim, D., and Jung, H., 2015, Deformation microstructures of olivine and chlorite in chlorite peridotites from Almklovdalen in the Western Gneiss Region, southwest Norway, and implications for seismic anisotropy: *International Geology Review*, v. 57, no. 5–8, p. 650–668.
- Kim, Y., Clayton, R. W., Asimow, P. D., and Jackson, J. M., 2013, Generation of talc in the mantle wedge and its role in subduction dynamics in central Mexico: *Earth and Planetary Science Letters*, v. 384, p. 81–87.
- Klemd, R., Gao, J., Li, J.-L., and Meyer, M., 2015, Metamorphic evolution of (ultra)-high-pressure subduction-related transient crust in the South Tianshan Orogen (Central

Asian Orogenic Belt): Geodynamic implications:
Gondwana Research, v. 28, no. 1, p. 1–25.

Konopelko, D., Kullerud, K., Apayarov, F., Sakiev, K., Baruleva, O., Ravana, E., and Lepekhina, E., 2012, SHRIMP zircon chronology of HP–UHP rocks of the Makbal metamorphic complex in the Northern Tien Shan, Kyrgyzstan: Gondwana Research, v. 22, no. 1, p. 300–309.

Kotková, J., O'Brien, P. J., and Ziemann, M. A., 2011, Diamond and coesite discovered in Saxony–type granulite: Solution to the Variscan garnet peridotite enigma: Geology, v. 39, no. 7, p. 667–670.

Kröner, A., Alexeiev, D. V., Rojas–Agramonte, Y., Hegner, E., Wong, J., Xia, X., Belousova, E., Mikolaichuk, A. V., Seltmann, R., Liu, D., and Kiselev, V. V., 2013, Mesoproterozoic (Grenville–age) terranes in the Kyrgyz North Tianshan: Zircon ages and Nd–Hf isotopic constraints on the origin and evolution of basement blocks in the southern Central Asian Orogen: Gondwana Research, v. 23, no. 1, p. 272–295.

Kröner, A., Windley, B. F., Badarch, G., Tomurtogoo, O., Hegner, E., Jahn, B. M., Gruschka, S., Khain, E. V., Demoux, A., Wingate, M. T., and McBride, J. H., 2007, Accretionary growth and crust formation in the Central Asian Orogenic Belt and comparison with the Arabian–Nubian shield: 4–D Framework of Continental Crust: Geological Society of America Memoir, v. 200, p. 181–209.

- Liou, J. G., and Zhang, R. Y., 1995, Significance of ultrahigh-P talc-bearing eclogitic assemblages, *Mineralogical Magazine*, Volume 59, p. 93–102.
- Long, L., Gao, J., Klemd, R., Beier, C., Qian, Q., Zhang, X., Wang, J., and Jiang, T., 2011, Geochemical and geochronological studies of granitoid rocks from the Western Tianshan Orogen: implications for continental growth in the southwestern Central Asian Orogenic Belt: *Lithos*, v. 126, no. 3, p. 321–340.
- Long, M. D., and Silver, P. G., 2008, The subduction zone flow field from seismic anisotropy: A global view: *science*, v. 319, no. 5861, p. 315–318.
- Long, M. D., and van der Hilst, R. D., 2006, Shear wave splitting from local events beneath the Ryukyu arc: trench-parallel anisotropy in the mantle wedge: *Physics of the earth and planetary interiors*, v. 155, no. 3, p. 300–312.
- Mainprice, D., 1990, A FORTRAN program to calculate seismic anisotropy from the lattice preferred orientation of minerals: *Computers & Geosciences*, v. 16, no. 3, p. 385–393.
- Mainprice, D., Barruol, G., and Ismail, W. B., 2000, The seismic anisotropy of the Earth's mantle: from single crystal to polycrystal: *Earth's Deep Interior: Mineral physics and tomography from the atomic to the global scale*, p. 237–264.

- Mainprice, D., and Ildefonse, B., 2009, Seismic anisotropy of subduction zone minerals—contribution of hydrous phases, *Subduction zone geodynamics*, Springer, p. 63–84.
- Mainprice, D., Le Page, Y., Rodgers, J., and Jouanna, P., 2008, Ab initio elastic properties of talc from 0 to 12 GPa: Interpretation of seismic velocities at mantle pressures and prediction of auxetic behaviour at low pressure: *Earth and Planetary Science Letters*, v. 274, no. 3, p. 327–338.
- McSkimin, H., Andreatch Jr, P., and Thurston, R., 1965, Elastic moduli of quartz versus hydrostatic pressure at 25 and 195.8 C: *Journal of Applied Physics*, v. 36, no. 5, p. 1624–1632.
- Meyer, M., Klemd, R., Hegner, E., and Konopelko, D., 2014, Subduction and exhumation mechanisms of ultra-high and high-pressure oceanic and continental crust at Makbal (Tianshan, Kazakhstan and Kyrgyzstan): *Journal of Metamorphic Geology*, v. 32, no. 8, p. 861–884.
- Meyer, M., Klemd, R., and Konopelko, D., 2013, High-pressure mafic oceanic rocks from the Makbal Complex, Tianshan Mountains (Kazakhstan & Kyrgyzstan): Implications for the metamorphic evolution of a fossil subduction zone: *Lithos*, v. 177, p. 207–225.
- Misra, S., Boutareaud, S., and Burg, J.-P., 2014, Rheology of talc sheared at high pressure and temperature: a case study for hot subduction zones: *Tectonophysics*, v. 610, p. 51–62.

- Mookherjee, M., and Capitani, G. C., 2011, Trench parallel anisotropy and large delay times: Elasticity and anisotropy of antigorite at high pressures: *Geophysical research letters*, v. 38, no. 9.
- Mookherjee, M., and Mainprice, D., 2014, Unusually large shear wave anisotropy for chlorite in subduction zone settings: *Geophysical Research Letters*, v. 41, no. 5, p. 1506–1513.
- Mookherjee, M., and Stixrude, L., 2009, Structure and elasticity of serpentine at high-pressure: *Earth and Planetary Science Letters*, v. 279, no. 1, p. 11–19.
- Moore, D. E., and Lockner, D. A., 2008, Talc friction in the temperature range 25°–400° C: Relevance for Fault-Zone Weakening: *Tectonophysics*, v. 449, no. 1–4, p. 120–132.
- Moore, D. E., and Lockner, D. A., 2011, Frictional strengths of talc-serpentine and talc-quartz mixtures: *Journal of Geophysical Research*, v. 116, no. B1.
- Moore, D. E., and Rymer, M. J., 2007, Talc-bearing serpentinite and the creeping section of the San Andreas fault: *Nature*, v. 448, no. 7155, p. 795–797.
- Muto, J., Hirth, G., Heilbronner, R., and Tullis, J., 2011, Plastic anisotropy and fabric evolution in sheared and recrystallized quartz single crystals: *Journal of Geophysical Research*, v. 116, no. B2.

- Nishizawa, O., and Yoshino, T., 2001, Seismic velocity anisotropy in mica-rich rocks: an inclusion model: *Geophysical Journal International*, v. 145, no. 1, p. 19–32.
- Ohuchi, T., Kawazoe, T., Nishihara, Y., and Irifune, T., 2012, Change of olivine a-axis alignment induced by water: Origin of seismic anisotropy in subduction zones: *Earth and Planetary Science Letters*, v. 317, p. 111–119.
- Ohuchi, T., Nishihara, Y., Seto, Y., Kawazoe, T., Nishi, M., Maruyama, G., Hashimoto, M., Higo, Y., Funakoshi, K.-i., Suzuki, A., Kikegawa, T., and Irifune, T., 2015, In situ observation of crystallographic preferred orientation of deforming olivine at high pressure and high temperature: *Physics of the Earth and Planetary Interiors*, v. 243, p. 1–21.
- Orozbaev, R., Hirajima, T., Bakirov, A., Takasu, A., Maki, K., Yoshida, K., Sakiev, K., Bakirov, A., Hirata, T., Tagiri, M., and Togonbaeva, A., 2015, Trace element characteristics of clinozoisite pseudomorphs after lawsonite in talc-garnet-chloritoid schists from the Makbal UHP Complex, northern Kyrgyz Tian-Shan: *Lithos*, v. 226, p. 98–115.
- Padrón-Navarta, J. A., Tommasi, A., Garrido, C. J., and López Sánchez-Vizcaíno, V., 2012, Plastic deformation and development of antigorite crystal preferred orientation in high-pressure serpentinites: *Earth and Planetary Science Letters*, v. 349, p. 75–86.

- Park, J., and Levin, V., 2002, Seismic anisotropy: tracing plate dynamics in the mantle: *Science*, v. 296, no. 5567, p. 485–489.
- Pawley, A. R., and Wood, B. J., 1995, The high–pressure stability of talc and 10 Å phase: potential storage sites for H₂O in subduction zones: *American Mineralogist*, v. 80, no. 9, p. 998–1003.
- Peacock, S. M., and Hyndman, R. D., 1999, Hydrous minerals in the mantle wedge and the maximum depth of subduction thrust earthquakes: *Geophysical Research Letters*, v. 26, no. 16, p. 2517–2520.
- Silver, P. G., and Chan, W. W., 1991, Shear wave splitting and subcontinental mantle deformation: *Journal of Geophysical Research: Solid Earth*, v. 96, no. B10, p. 16429–16454.
- Poli, S., and Schmidt, M., 1997, The high–pressure stability of hydrous phases in orogenic belts: an experimental approach on eclogite–forming processes: *Tectonophysics*, v. 273, no. 1, p. 169–184.
- Russo, R., and Silver, P., 1994, Trench–parallel flow beneath the Nazca plate from seismic anisotropy: *Science*, v. 263, no. 5150, p. 1105–1111.
- Song, T.–R. A., and Kim, Y., 2012, Localized seismic anisotropy associated with long–term slow–slip events beneath southern Mexico: *Geophysical Research Letters*, v. 39, no. 9, p. L09308.

Tagiri, M., Takiguchi, S., Ishida, C., Noguchi, T., Kimura, M., Bakirov, A., Sakiev, K., Takahashi, M., Takasu, A., and Bakirov, A., 2010, Intrusion of UHP metamorphic rocks into the upper crust of Kyrgyzian Tien–Shan: PT path and metamorphic age of the Makbal Complex: *Journal of mineralogical and petrological sciences*, v. 105, no. 5, p. 233–250.

Togonbaeva, A., Takasu, A., Bakirov, A. A., Sakurai, T., Tagiri, M., Bakirov, A. B., and Sakiev, K., 2009, CHIME monazite ages of garnet–chloritoid–talc schists in the Makbal Complex, Northern Kyrgyz Tien–Shan: First report of the age of the UHP metamorphism: *Journal of Mineralogical and Petrological Sciences*, v. 104, no. 2, p. 77–81.

Ulmer, P., and Trommsdorff, V., 1995, Serpentine Stability to Mantle Depths and Subduction–Related Magmatism: *Science*, v. 268, p. 858–861.

Vaughan, M. T., and Guggenheim, S., 1986, Elasticity of muscovite and its relationship to crystal structure: *Journal of Geophysical Research: Solid Earth (1978–2012)*, v. 91, no. B5, p. 4657–4664.

Vinnik, L. P., Aleshin, I. M., Kaban, M. K., Kiselev, S. G., Kosarev, G. L., Oreshin, S. I., and Reigber, C., 2006, Crust and mantle of the Tien Shan from data of the receiver function tomography: *Izvestiya, Physics of the Solid Earth*, v. 42, no. 8, p. 639–651.

- Wang, X., Zeng, Z., Liu, C., Chen, J., Yin, X., Wang, X., Chen, D., Zhang, G., Chen, S., Li, K., and Ouyang, H., 2009, Talc-bearing serpentized peridotites from the southern Mariana forearc: implications for aseismic character within subduction zones: *Chinese Journal of Oceanology and Limnology*, v. 27, no. 3, p. 667–673.
- Watanabe, T., Shirasugi, Y., and Michibayashi, K., 2014, A new method for calculating seismic velocities in rocks containing strongly dimensionally anisotropic mineral grains and its application to antigorite-bearing serpentinite mylonites: *Earth and Planetary Science Letters*, v. 391, p. 24–35.
- Wei, C., and Powell, R., 2006, Calculated phase relations in the system NCKFMASH (Na₂O–CaO–K₂O–FeO–MgO–Al₂O₃–SiO₂–H₂O) for high-pressure metapelites: *Journal of Petrology*, v. 47, no. 2, p. 385–408.
- Wenk, H.-R., Kanitpanyachoen, W., and Voltolini, M., 2010, Preferred orientation of phyllosilicates: Comparison of fault gouge, shale and schist: *Journal of Structural Geology*, v. 32, no. 4, p. 478–489.
- Wilke, F. D. H., O'Brien, P. J., Schmidt, A., and Ziemann, M. A., 2015, Subduction, peak and multi-stage exhumation metamorphism: Traces from one coesite-bearing eclogite, Tso Moriri, western Himalaya: *Lithos*, v. 231, p. 77–91.
- Windley, B., Allen, M., Zhang, C., Zhao, Z., and Wang, G., 1990, Paleozoic accretion and Cenozoic reformation of the

- Chinese Tien Shan range, central Asia: *Geology*, v. 18, no. 2, p. 128–131.
- Winter, J. D., 2010, *Principles of igneous and metamorphic petrology*, Prentice Hall New York.
- Wolfe, C. J., and Vernon, F. L., 1998, Shear–wave splitting at central Tien Shan: Evidence for rapid variation of anisotropic patterns: *Geophysical Research Letters*, v. 25, no. 8, p. 1217–1220.
- Xiao, W., and Santosh, M., 2014, The western Central Asian Orogenic Belt: a window to accretionary orogenesis and continental growth: *Gondwana Research*, v. 25, no. 4, p. 1429–1444.
- Zhang, S., and Karato, S.-i., 1995, Lattice preferred orientation of olivine aggregates deformed in simple shear: *Nature*, v. 375, no. 6534, p. 774–777.
- Zhou, J.-B., and Wilde, S. A., 2013, The crustal accretion history and tectonic evolution of the NE China segment of the Central Asian Orogenic Belt: *Gondwana Research*, v. 23, no. 4, p. 1365–1377.

국문 초록

활석은 섭입대의 맨틀 윗지와 섭입한 해양판에서 형성되는 중요한 합수 관상광물 중 하나이다. 합수광물은 일부 섭입대에서 나타나는 높은 값의 지진파 비등방성과 이로 인한 긴 S파 지연시간 (delay time) 을 설명할 수 있다고 연구되어왔다. 특히 합수광물이 강한 격자선호방향 (LPO; Lattice preferred orientation) 을 나타낼 경우 상부 맨틀과 섭입판에서의 지진파 비등방성을 설명할 수 있다고 알려져 있다. 그러나 자연상에서 변형된 활석에 대해서는 지금까지 격자선호방향이 보고된 바가 없다. 따라서 이번 연구에서는 고압에서 변형 및 변성작용을 받은 편암 내에 존재하는 다결정질 활석의 격자선호방향을 측정하였다. 또한 압력에 따른 활석 단결정의 탄성계수를 적용하여, 몇 개의 압력조건에서 활석이 나타낼 지진파 비등방성을 계산해보았다. 활석이 나타내는 격자선호방향을 측정한 결과, [001] 축은 편암의 엽리에 아수직하게 강한 배열을 보였다. 그리고 활석의 [100] 축과 [010] 축은 편암의 엽리에 아평행하게 약한 거들을 보임과 동시에, 강도는 약하지만 특정 방향으로 배열이 집중되는 경향성을 보여주었다. 활석의 격자선호방향 측정결과를 이용하여 활석의 지진파 비등방성을 계산한 결과, 다결정질 활석의 지진파 비등방성은 그 크기가 매우 컸으며 (P파에 대해서 68-69 %, S파에 대해서 21-23 %), 압력이 높아짐에 따라 지진파 비등방성의 크기는 작아졌다. 한편 엽리를 수직으로 통과하는 빠른 S파가 나타내는 편광 방향을 계산한 결과, 섭입대의 섭입각 (dipping angle) 이 30도 이상이면 활석은 해구에 평행한 S파 편광을 나타냈다. 또한 이는 활석의 [100] 축과 [010] 축의 격자선호방향에 따라 다소 차이를 보였다.

이러한 결과들에 의하면, 주된 맨틀 구성광물인 감람석만으로는 해석하기 어려운 1-2 초 가량의 긴 S파 지연시간을 섭입대 내 활석의 강한 격자선호방향의 영향으로 설명할 수 있다. 또한 활석의 격자선호방향은 지구상의 많은 섭입대에서 해구와 평행하게 관측되는 빠른 S파 편광방향을 설명할 수 있는 하나의 중요한 요인이 될 수 있다.

주요어 : 활석, 격자선호방향, 지진파 비등방성, 섭입대

학 번 : 2014-20324